Article:
Liu, J., Feng, S., Wang, T. et al. (4 more authors) (2026) Shakedown limit analysis for heavy-haul railway tracks. Transportation Geotechnics, 56. 101741. ISSN: 2214-3912

https://doi.org/10.1016/j.trgeo.2025.101741

Shakedown Limit Analysis for Heavy-Haul Railway Tracks

Jinglei Liu[1,2], Shiqi Feng[1], Tengfei Wang[3], David P. Connolly [4], Jing Guo[5], Erjun Guo[5], Qingzhi Ye [1,6,*]

1. School of Civil Engineering, Hebei University of Architecture, Zhangjiakou 075000, China
2. Hebei Key Laboratory of Diagnosis, Reconstruction and Anti-disaster of Civil Engineering, Zhangjiakou 075000, China
3. MOE Key Laboratory of High-Speed Railway Engineering, School of Civil Engineering, Southwest Jiaotong University, Chengdu, 610031, China
4. School of Civil Engineering, University of Leeds, Leeds LS2 9JT, UK
5. China Construction Eighth Engineering Division Rail Transit Construction CO. LTD, Nanjing, China
6. Hebei Innovation Center of Transportation Infrastructure in Cold Region, Hebei University of Architecture, Zhangjiakou, 075000, China

*Corresponding author: yqz2280@hebiace.edu.cn (Q. Ye)

Abstract

The lower-bound shakedown theorem provides a crucial framework for evaluating the long-term stability of structures subjected to cyclic loading by defining both the shakedown limit and critical depth. However, its application in freight railway engineering remains relatively limited. To overcome this gap, shakedown theory has been integrated into the design of heavy-haul railway trackbed systems, enabling assessment of substructure stability under repeated loading. The stress distributions along the longitudinal and transverse axes of the sub-ballast surface, induced by a four-axle loading pattern, were quantified and validated through Gaussian curve fitting. Additionally, a methodology based on the Mohr–Coulomb yield criterion was developed to estimate the shakedown limit of the subgrade, employing the corresponding shakedown axle load as the primary evaluation index. Parametric analyses examined the effects of three key design parameters: the internal friction angle of the sub-ballast, the elastic modulus of the engineered subgrade, and the thickness ratio between the sub-ballast and engineered subgrade. Findings consistently showed that increases in these parameters lead to higher shakedown axle loads. Among them, the internal friction angle of the sub-ballast has the most pronounced influence, whereas the thickness ratio plays a relatively minor role. For example, elevating the internal friction angle from 25° to 40° produces a significant 48.0% rise in the shakedown axle load, highlighting its pivotal contribution to enhancing the substructure's resilience against cyclic loads.

Keywords: Heavy-haul railway; Lower-bound shakedown theorem; Four-axle load pattern; Gaussian function; Shakedown axle load

1. Introduction

Heavy-haul railways offer distinct advantages, including high capacity, operational efficiency, low energy consumption, and economic viability, making them integral to global freight transportation[1]. In recent years, increased axle loads and train speeds has exacerbated cumulative plastic deformation within the substructure, posing significant risks to the safety of freight operations[2]. Consequently, controlling this deformation is vital to ensuring the enduring stability and reliable service performance of heavy-haul railway infrastructure.

Shakedown theory provides a systematic framework for evaluating the long-term deformation behaviour of structures subjected to cyclic loading by establishing both the shakedown limit and its associated critical depth[3-4]. This theory has found extensive application in road engineering, railway substructures, and underground infrastructure, and is routinely employed in the design of both ballasted and ballastless high-speed railways[5-10]. In contrast to high-speed railways, which require stringent deformation limits for ride comfort, heavy-haul railways permit limited plastic deformation within the substructure. Accordingly, the lower-bound shakedown theorem serves as an effective approach for restricting substructure deformation to within the elastic shakedown regime.

First proposed by Melan in 1938, the lower-bound shakedown theorem provides a foundational framework for evaluating the elastoplastic behaviour of structures subjected to repeated or moving loads[11]. The theorem identifies a critical load threshold—the shakedown limit—below which the structure undergoes limited initial plastic deformation before reaching a stable state. This initial plasticity generates a self-equilibrating residual stress field that prevents further plastic flow, enabling the structure to respond elastically during subsequent loading cycles.

In pavement engineering, shakedown theory has seen substantial development. Early studies focused on residual stress distributions in semi-infinite media. Radovsky and Murashina[12] first revealed the depth-dependent variation of the residual stress field. Wang and Yu[13-14] subsequently validated the universality of this distribution across various soils through numerical simulations. The research then progressed to multilayer systems. Brown et al.[15] conducted moving wheel load tests on two- and three-layer pavement systems, demonstrating

the applicability of the three-dimensional lower-bound shakedown theory to multilayer configurations. Shiau and Yu[16] developed an approach to estimate the shakedown limit in layered structures by incorporating the combined effects of elastic and residual stress fields. Building upon this foundation, subsequent research has explored how key material and structural parameters affect shakedown behaviour. For example, Sun et al.[17] examined the roles of surface friction coefficient, layer thickness, load distribution, and internal friction angle within a dual-layer pavement system, verifying the reliability of the proposed approach. Expanding on this work, Yu and Wang[18-19] formulated rigorous lower-bound shakedown solutions for cohesive-frictional half-spaces exposed to three-dimensional moving loads, highlighting the critical influence of contact area geometry and material characteristics on shakedown behaviour. Acknowledging the widespread anisotropy in pavement materials, Wang and Yu[20] subsequently introduced the first lower-bound shakedown solution tailored for anisotropic cohesive-frictional half-spaces subjected to three-dimensional surface loading. This advancement corrected the limitations of traditional isotropic assumptions, producing results that more accurately reflect actual engineering conditions. Building on this refinement, Wang and Yu[21] derived a unified shakedown limit equation applicable to both flexible and rigid pavements, as well as ballasted and ballastless track systems, clarifying the combined influence of material properties, loading characteristics, and self-weight. In addition, Wang and Yu[22] established a numerical analysis framework for evaluating the shakedown limits of flexible pavement structures and introduced a simplified method to facilitate its application in practical engineering scenarios. Qian et al.[23], employing Melan's theorem alongside finite and infinite element methods, analysed dynamic shakedown behaviour under rolling–sliding contact, demonstrating that both velocity and friction coefficient significantly influence shakedown performance. Taken together, these studies have significantly contributed to both the theoretical advancement and practical implementation of shakedown theory in pavement engineering, establishing a solid basis for assessing the long-term stability of multilayered structures under complex loading conditions.

Within the field of railway engineering, Zhuang and Wang[24-26] incorporated shakedown theory into the analysis of ballasted track systems for high-speed railways. Their studies

investigated the influence of key parameters such as the wheel–rail interface friction coefficient, ballast stiffness, and various layer configurations on the shakedown performance of the track structure. Later studies by Wang et al.[7,27] extended the framework to ballastless tracks, including continuous slab structures and those with expansion joints. These studies highlighted the combined influences of friction angle, modulus, and subbase thickness under dynamic loading. Furthermore, the concept of the "shakedown axle load" emerged as a key metric, representing the highest axle load under which no cumulative plastic deformation occurs when subjected to repeated loading. It incorporates load type, speed, and material characteristics and has proven vital in evaluating track performance. Recent studies have substantially advanced the understanding of ballast shakedown behaviour. Xiao et al. [28-29] developed a high-fidelity discrete element model capable of capturing the irregular geometry and breakage characteristics of ballast particles, employing laser scanning technology for precise particle representation. The model was calibrated and validated using cyclic triaxial tests, systematically elucidating ballast deformation characteristics and shakedown limits under varying load amplitudes, particle properties, and loading frequencies. The findings categorised ballast deformation into three distinct states: plastic shakedown, plastic creep, and incremental collapse. Gomes et al. [30] introduced a theoretical framework for shakedown analysis, demonstrating that once ballast achieves a shakedown state, its cumulative permanent deformation stabilises, thereby supporting the long-term preservation of track geometry. Wang et al. [31] utilised a three-dimensional finite element model of a multilayered foundation system, coupled with Melan’s lower-bound shakedown theorem, to assess the effects of friction angle, modulus ratio, and thickness ratio on shakedown limits. A predictive function for shakedown load was proposed, introducing the concept of a "shakedown axle load" to capture the combined influence of material properties and train speed. Furthermore, Zhuang et al. [3] extended three-dimensional shakedown analysis to railway structures subjected to multiple Hertzian contact loads, systematically investigating the ballast layer’s mechanical response and shakedown criteria under combined wheel loads, thereby improving the understanding of in-service track behaviour under complex loading conditions.

Despite its success in high-speed railways, shakedown research in heavy-haul contexts

remains limited. Load models derived from high-speed track systems are not directly applicable to the operational conditions of heavy-haul railways. Furthermore, the discrete placement of sleepers in heavy-haul railway systems significantly influences the dynamic stress patterns observed on the subgrade surface. Consequently, it becomes essential to develop load distribution models tailored specifically for heavy-haul substructures, which consider the distinctive diffusion characteristics of heavy axle loads within the trackbed. Heavy-haul trains, distinguished by their substantial load-bearing capacity, high cargo density, large axle weights, short axle spacing, and relatively reduced train length[32], generate a unique stress field arising from the four axles of two bogies during each full loading–unloading cycle. This stress pattern differs considerably from that observed in high-speed railways. Additionally, the dynamic stress response exhibited by heavy-haul railway subgrades is characterized by more complex and significant nonlinear behaviours compared to those commonly seen in high-speed rail systems[33-34]. Lv et al.[35] used Gaussian functions to analyse sleeper load-sharing ratios, indicating much higher stress levels under four-axle loading than those under single-axle loading. Mei et al.[36] and Liu et al.[37-38] further demonstrated that peak dynamic stress approximately follows a normal and bimodal distribution in longitudinal and transverse directions, respectively. However, current load models still fail to fully reflect the dynamic stress patterns observed in operational heavy-haul railways. A more representative sub-ballast surface loading model, reflecting the specific loading conditions of heavy-haul railways, is therefore urgently required.

To address this， the present study develops a comprehensive method for shakedown analysis of ballasted substructures under four-axle loading in heavy-haul systems. A three-dimensional finite element model is developed to analyze the stress distribution on the sub-ballast surface subjected to four-axle loading. This is followed by layered modelling, enabling the extraction of elastic stress fields within each structural layer. The shakedown limit and critical depth are then determined through an iterative approach. Parametric sensitivity analyses assess the influence of internal friction angle, elastic modulus, and train speed on shakedown performance. The shakedown axle load is employed as the principal evaluation index, supporting the development of optimisation design for heavy-haul railway systems based on

shakedown theory.

2. Shakedown theory and calculation method

2.1 Lower bound shakedown theorem

When subjected to cyclic loading, a structure may experience either elastic or plastic deformation, primarily governed by the magnitude of the applied load. As shown in Figure 1, when the cyclic load stays within the material's elastic limit, the structural behaviour remains fully elastic. However, when the load surpasses this elastic threshold but does not exceed the elastic shakedown limit, the structure undergoes initial yielding accompanied by limited plastic deformation. This early-stage plasticity leads to the development of a self-equilibrating residual stress field, which effectively restrains further plastic evolution under subsequent load cycles, allowing the structure to return to an elastic response—commonly referred to as the elastic shakedown state. In contrast, when the cyclic load surpasses the elastic shakedown limit but stays below the plastic shakedown limit, the residual stress field fails to prevent the ongoing accumulation of plastic deformation. Consequently, plastic deformation develops incrementally with each load cycle, eventually leading to structural failure due to excessive accumulated strain. Once the cyclic load surpasses the plastic shakedown limit, extensive plastic deformation develops rapidly, resulting in structural collapse, a phenomenon commonly referred to as "ratcheting failure".

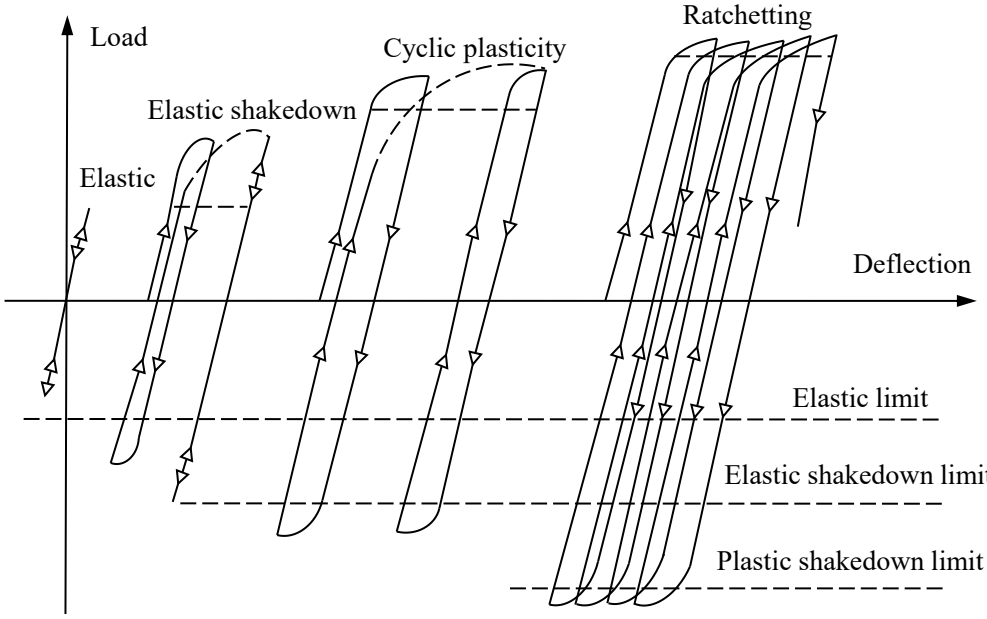

Figure 1. Elastic–perfectly plastic structural response under cyclic loading[8,39].

Maintaining the long-term stability of heavy-haul railway substructures requires that the structural response remain confined to the elastic shakedown state. Under these conditions, the total stress field comprises three primary components: the geostatic stress field due to self-weight, the residual stress field arising from initial plastic deformation, and the elastic stress field resulting from external loads. According to Melan's lower-bound shakedown theorem, the residual stress field is time-invariant and satisfies the self-equilibrium condition[21]. To ensure that the structure operates within the elastic shakedown regime, the total stress field must conform to the inequality constraint defined by the Mohr–Coulomb yield criterion, as presented in Equation (1):

$$f(\lambda\sigma_{ij}^{e}+\sigma_{ij}^{0}+\sigma_{ij}^{r})\le 0 \tag{1}$$

where $f(\cdot)$ represents the yield criterion; σ_{ij}^{e} denotes the elastic stress field produced by a unit cyclic load; λ is the load amplification factor; $\lambda\sigma_{ij}^{e}$ corresponds to the elastic stress field arising from external loading; i and j are the coordinate indices associated with the vertical direction and the direction of load movement within the semi-infinite domain, respectively; σ_{ij}^{0} refers to the geostatic stress field resulting from self-weight; and σ_{ij}^{r} represents the residual stress field.

2.2 Shakedown solution for half-space

As shown in Figure 2, a moving load λP travels along the surface of a homogeneous semi-infinite medium at a constant velocity v. If the structure remains within the elastic shakedown state under such external loading, the residual stress field is self-equilibrating and remains unaffected by the duration of loading. When the load amplification factor increases to its maximum value, denoted as λ_{sd}, which satisfies the yield criterion, a distinct residual stress field develops at the critical depth. The corresponding external load, expressed as $P_{sd}=\lambda_{sd}P$, defines the shakedown limit. Accurate determination of this limit necessitates constructing a residual stress field that guarantees the total stress field continuously satisfies the Mohr–Coulomb yield inequality outlined in Equation (1) throughout the entire loading cycle.

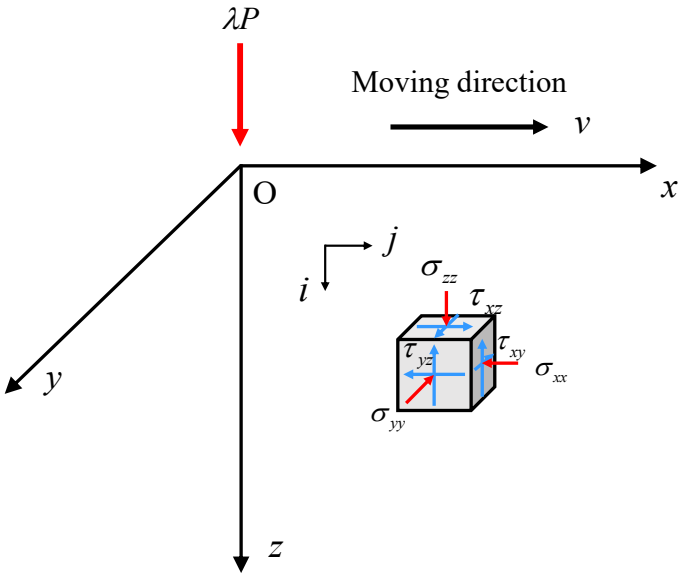

Figure 2. Homogeneous half-space subjected to a vertically applied moving load.

In a homogeneous semi-infinite domain, the critical plane is oriented parallel to the direction of load movement, with $y = 0$ identified as the principal plane for evaluating structural stability and integrity under loading conditions[18-21]. Accordingly, y = 0 is adopted in this study as the reference plane for conducting shakedown analysis of the substructure. The elastic stress field induced by the moving load comprises three primary components: σ_{xx}^{e}, σ_{zz}^{e} and τ_{xz}^{e}. In contrast, the residual stress field consists solely of the normal stress component σ_{xx}^{r}. The self-weight stress field—also known as the geostatic stress field—includes components σ_{xx}^{0} and σ_{zz}^{0} [7]. The lateral stress is determined using the coefficient of earth pressure, expressed as $k=\mu/(1-\mu)$, where μ represents Poisson's ratio. The explicit expressions for the geostatic stress field components are presented in Equation (2).

$$\begin{cases} \sigma_{zz}^{0} = \gamma z \\ \sigma_{xx}^{0} = k\sigma_{zz}^{0} = \dfrac{\mu}{1-\mu}\gamma z \end{cases} \tag{2}$$

Where γ denotes the unit weight of the soil, and z denotes the vertical depth.

The total stress field is determined in accordance with Equation (3).

$$\begin{cases} \sigma_{xx} = \lambda\sigma_{xx}^{e} + \sigma_{xx}^{0} + \sigma_{xx}^{r} \\ \sigma_{zz} = \lambda\sigma_{zz}^{e} + \sigma_{zz}^{0} \\ \tau_{xz} = \lambda\tau_{xz}^{e} \end{cases} \tag{3}$$

By substituting the total stress field into inequality (1), the total stress field defined in Equation (3) must satisfy the yield condition specified in Equation (1). Assuming that the structural backfill conforms to the Mohr–Coulomb yield criterion, the lower-bound shakedown

theorem requires that the maximum principal stress σ_1 and the minimum principal stress σ_3, derived from the total stress field, meet the condition expressed in Equation (4).

$$(\sigma_1-\sigma_3)+(\sigma_1+\sigma_3)\sin\varphi-2c\cos\varphi\le 0 \tag{4}$$

Here, c denotes the soil cohesion (Pa), and φ represents the internal friction angle (°). The principal stresses σ_1 and σ_3 are computed according to Equation (5):

$$\begin{cases}\sigma_1=\dfrac{\sigma_{xx}+\sigma_{zz}}{2}+\sqrt{\left(\dfrac{\sigma_{xx}-\sigma_{zz}}{2}\right)^2+\tau_{xz}^2}\\ \sigma_3=\dfrac{\sigma_{xx}+\sigma_{zz}}{2}-\sqrt{\left(\dfrac{\sigma_{xx}-\sigma_{zz}}{2}\right)^2+\tau_{xz}^2}\end{cases} \tag{5}$$

Substituting Equation (5) into Equation (4) results in Inequality (6).

$$\begin{aligned}&\sqrt{\left(\lambda\sigma_{xx}^{e}+\sigma_{xx}^{0}+\sigma_{xx}^{r}-\lambda\sigma_{zz}^{e}-\sigma_{zz}^{0}\right)^2+4\left(\tau_{xz}^{e}\right)^2}\\&-\left(\lambda\sigma_{xx}^{e}+\sigma_{xx}^{0}+\sigma_{xx}^{r}+\lambda\sigma_{zz}^{e}+\sigma_{zz}^{0}\right)\sin\varphi-2c\cos\varphi\le 0\end{aligned} \tag{6}$$

By simplifying Inequality (6) and isolating the residual stress component σ_{xx}^{r}, Equation (7) is derived.

$$f=(\sigma_{xx}^{r}+M)^2+N\le 0 \tag{7}$$

where M and N are defined in Equation (8).

$$\begin{cases}M=\lambda(\sigma_{xx}^{e}-\sigma_{zz}^{e})+(\sigma_{xx}^{e}-\sigma_{zz}^{e})+2\tan\varphi[c-(\lambda\sigma_{zz}^{e}+\sigma_{zz}^{0})\tan\varphi]\\ N=4(1+\tan^2\varphi)[(\lambda\tau_{zz}^{e})^2-(c-(\lambda\sigma_{zz}^{e}+\sigma_{zz}^{0})\tan\varphi)^2]\end{cases} \tag{8}$$

Here, c denotes the cohesion, and φ represents the internal friction angle.

A sufficient but not necessary condition for Inequality (7) to have real roots is $N\le 0$, that is:

$$\lambda\le\frac{c-\sigma_{zz}^{0}\tan\varphi}{\left|\tau_{xz}^{e}\right|+\sigma_{zz}^{e}\tan\varphi} \tag{9}$$

According to Equation (6), within a semi-infinite medium, the vertical component of the geostatic stress remains constant at any specified depth $z=i$.

By identifying the maximum value of $|\tau_{xz}^{e}|+\sigma_{zz}^{e}\tan\varphi$ along the longitudinal (x) direction at this depth, the corresponding minimum load amplification factor $\{\lambda_i\}_{min}$ can be determined. Repeating this procedure across all depths and selecting the overall minimum yields the initial value λ_1 of the amplification factor λ. This value is a candidate for the shakedown limit but must be further verified. By applying the yield condition $f=0$, two possible residual stress solutions emerge at the coordinate position ($z=i$, $x=j$): the smaller root $-M_{ij}-\sqrt{-N_{ij}}$

and the larger root $-M_{ij}+\sqrt{-N_{ij}}$. For the yield condition to be satisfied, the residual stress at each depth $z=i$ must lie within the interval defined by the maximum value of the smaller roots and the minimum value of the larger roots, thereby ensuring compliance with the inequality presented in Equation (10).

$$\max(-M_{ij}-\sqrt{-N_{ij}})_{z=i} \le \sigma_{xx}^{r} \le \min(-M_{ij}+\sqrt{-N_{ij}})_{z=i} \tag{10}$$

When the minimum value of the larger residual stress root exceeds the maximum value of the smaller root, a real solution satisfying the yield condition $f \leqslant 0$ exists. This outcome indicates that the structure has achieved a shakedown state, as illustrated in Figure 3(a), where the initial amplification factor, $\lambda=\lambda_1$, corresponds to the shakedown limit. In contrast, if no feasible residual stress solution is identified, the structure fails to satisfy the shakedown condition, as demonstrated in Figure 3(b).

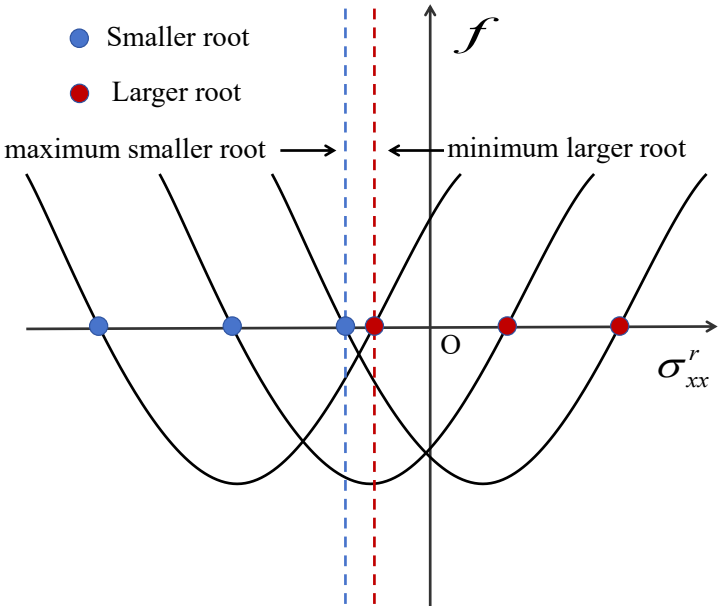

(a)

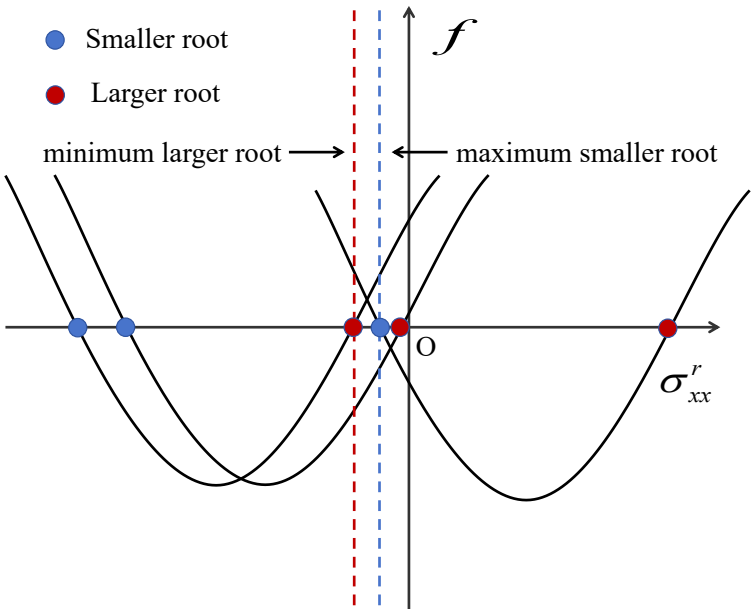

(b)

Figure 3. Shakedown criterion based on the residual stress field: (a) shakedown state; (b) non-shakedown state

2.3 Shakedown analysis of layered substructures

The preceding section detailed the procedure for determining the shakedown limit within a homogeneous semi-infinite medium. In contrast, the substructure of a heavy-haul railway consists of several homogeneous finite layers. In this context, the shakedown limit for each layer is determined using an iterative, layer-by-layer approach. The smallest value obtained from this process is regarded as the overall shakedown limit of the subgrade structure, as defined by Equation (11).

$$\lambda=\min\{\lambda_1,\lambda_2,\cdots,\lambda_n\} \tag{11}$$

In this equation, λ_i denotes the shakedown limit of the i^{th} structural layer, which is governed by the internal friction angle φ_i and the cohesion c_i of the corresponding soil layer.

Accurately assessing the elastic stress field generated by a unit external load is a crucial step in determining the shakedown limit for both semi-infinite and multilayered structural systems. In the layered substructure systems typical of heavy-haul railways, the distribution of elastic stresses is significantly influenced by the specific characteristics of train-induced loading. Conventional analytical approaches encounter significant limitations in accurately characterising the three-dimensional stress distribution arising from the superposition of multi-

axle loads. In contrast, the finite element method (FEM) offers a robust numerical framework for directly simulating the transverse and longitudinal stress distributions on the sub-ballast surface, thereby enabling the precise extraction of elastic stress components within each structural layer. The computational procedure comprises the following steps:

a) Determine the substructure loading pattern by solving the transverse and longitudinal stress distribution functions on the surface of the sub-ballast.

b) A multilayer finite element model is utilized to extract the elastic stress fields within each structural layer through numerical integration. These calculated stress fields are then superimposed upon the initial geostatic stress field, followed by application of the Mohr–Coulomb yield criterion to assess the residual stress field and identify the corresponding critical depth.

c) Calculate the load amplification factors λ_1， λ_2 and λ_3 for each layer, and define the minimum value as the global shakedown limit of the substructures.

The sequential procedure for determining the shakedown limit of the layered structure is schematically depicted in Figure 4.

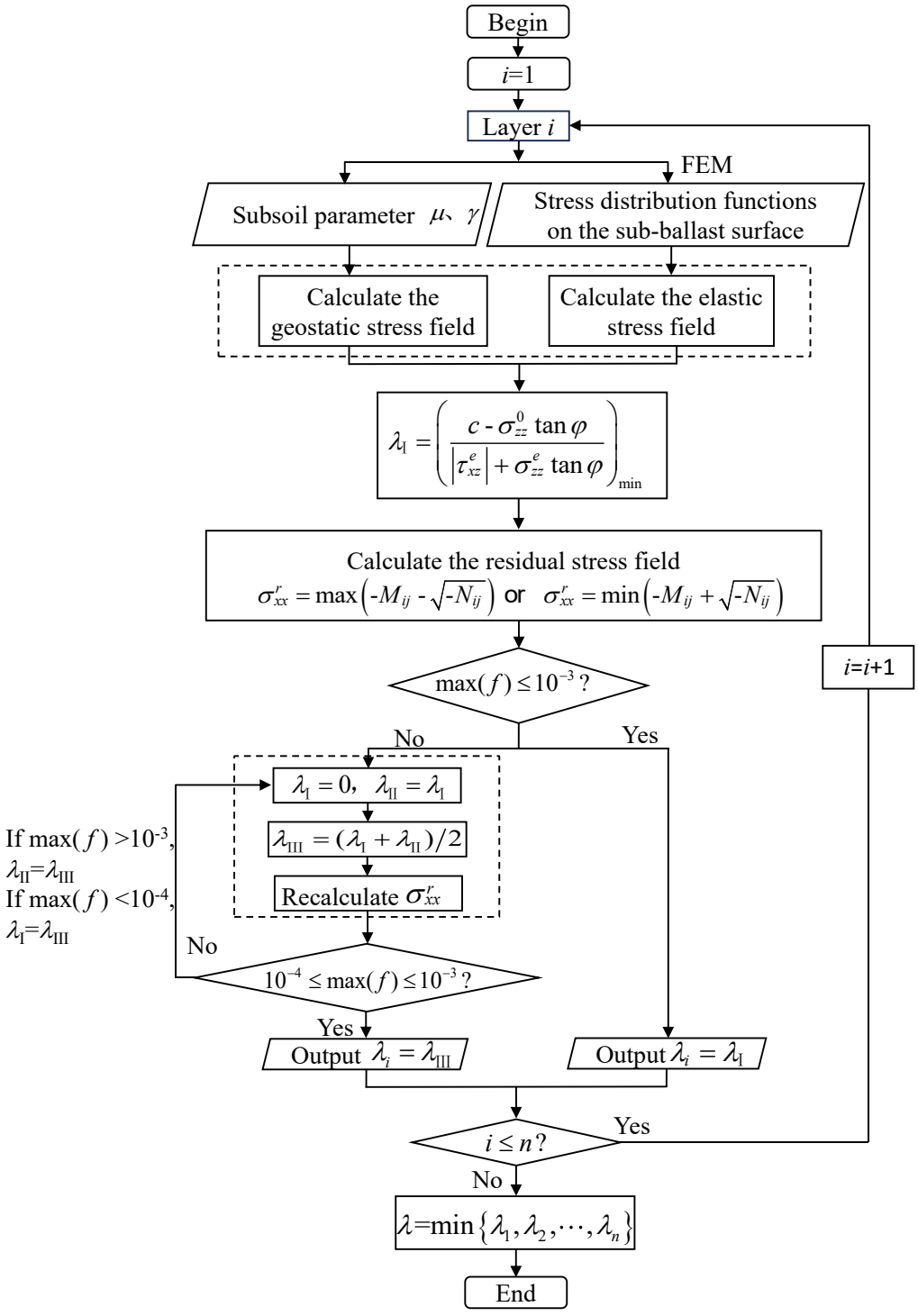

Figure 4. Flowchart of the shakedown solution

3. Finite element model of track structure

In the analysis of railway substructure shakedown limits, conventional methods such as the Boussinesq solution[40] have been widely used. However, shakedown analysis of heavy-haul railway subgrade structures remains limited. Due to the discontinuous distribution of sleepers

along the direction of train movement, the actual loading pattern and the resulting elastic stress field distribution are not yet fully understood. As discussed in Section 2.3, accurate determination of the shakedown limit for layered subgrade structures depends critically on the precise characterisation of the elastic stress field, which is fundamentally governed by the actual distribution of train loads on the surface of the sub-ballast.

To accurately replicate the load diffusion characteristics of heavy-haul trains within the subgrade structure, a finite element model representing the heavy-haul railway substructure was established. Numerical simulations were performed to extract the transverse and longitudinal loading patterns on the surface of the sub-ballast under four-axle loading. These simulation results, integrated with Melan's lower-bound shakedown theory, enabled the superposition of the elastic stress field generated by external moving loads onto the self-weight stress field of the substructure. An iterative calculation procedure was employed to determine the critical residual stress field capable of resisting plastic deformation, along with the corresponding critical depth. This methodology facilitates a systematic and comprehensive assessment of the long-term stability of the substructure.

3.1 Model development

In accordance with the Heavy-Haul Railway Design Code (TB 10625-2017)[41], a freight train characterized by a 35 t axle load and an operational speed of = 100 km/h was selected as the subject of this study. A three-dimensional finite element model of the track–substructure system was developed using Abaqus. This model, arranged sequentially from top to bottom, includes rails, fasteners, sleepers, ballast, sub-ballast, engineered subgrade, natural subgrade, and foundation soil. The detailed structural configuration of the heavy-haul railway subgrade is depicted in Figure 5.

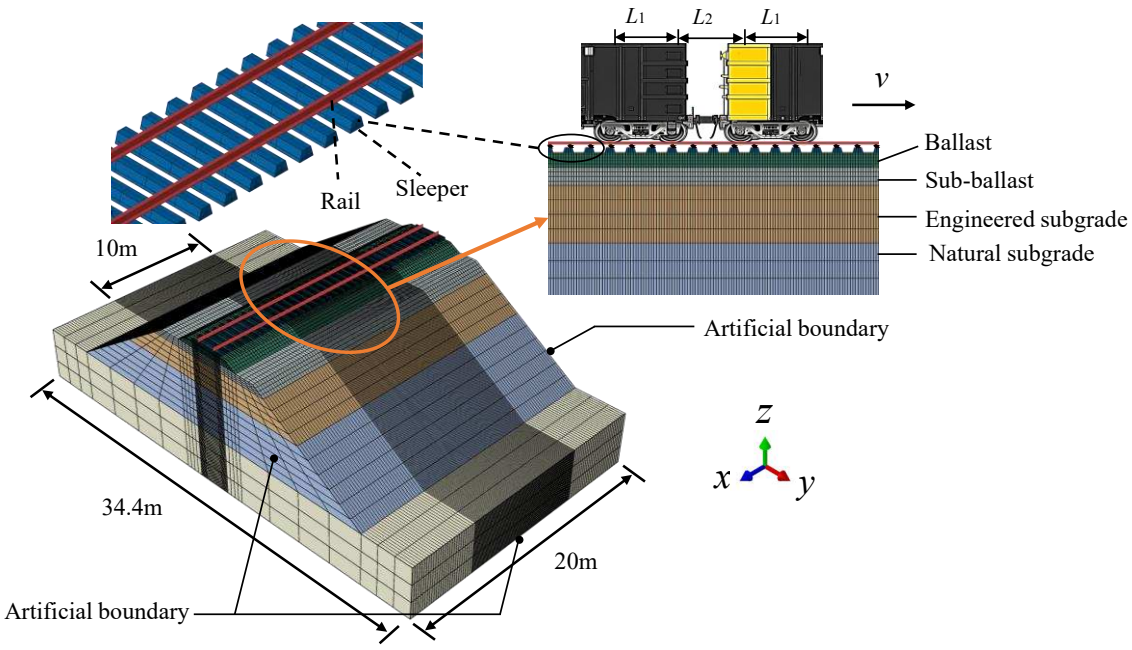

Figure 5. Finite element model of the heavy-haul railway

Concrete Type III sleepers were adopted in the model, featuring a trapezoidal cross-section with a top width of 0.2055 m, a bottom width of 0.32 m, and a height of 0.22 m. The sleepers were spaced at intervals of 0.6 m. The ballast layer featured a top width of 3.6 m, a bottom width of 5.35 m, and side slopes of 1:1.75. The sub-ballast layer measured 8.4 m in width and 0.6 m in thickness. The engineered subgrade was 1.9 m high, while the underlying natural subgrade extended to a height of 3.5 m with side slopes of 1:1.5. Standard Type 75 rails were incorporated into the model, with a track gauge of 1.435 m. To realistically replicate the wheel–rail interaction, the rails were connected to the sleepers via spring fasteners with a stiffness of 8,000 kN/m, spaced at intervals of 0.6 m. Due to the minimal relative sliding between sleepers, ballast, sub-ballast, subgrade, embankment, and foundation, tie constraints were applied at all contact interfaces to ensure coordinated deformation. These tie connections enforce zero relative displacement between surfaces, effectively capturing the cooperative behaviour of the layered track structure. A detailed description of these interactions has been incorporated into the revised manuscript. Sincere appreciation is extended for this insightful guidance. The material properties assigned to each structural component are summarised in Table 1[38].

Table 1. Material properties of the multilayer heavy-haul railway substructure

Components	Density (kg/m^3)	Modulus	Poisson's	Cohesion	Friction

		(MPa)	Ratio	(kPa)	angle (°)
Rail	7,850	210,000	0.25	—	—
Sleeper	2,500	30,000	0.2	—	—
Ballast	2,400	200	0.25	—	40
Sub-ballast	2,300	180	0.3	58	33
Engineered subgrade	2,200	150	0.3	45	31
Natural subgrade	1,800	70	0.35	30	17
Foundation	1,700	50	0.35	25	15

To minimise boundary reflection, viscoelastic artificial boundaries were applied along the model edges[42], and infinite elements were introduced in the far-field foundation to enhance energy dissipation. The model employed C3D8R hexahedral elements, with a total of 193,728 elements and 210,185 nodes. To improve computational efficiency, the moving element method was adopted[43], whereby the applied load moves within a stationary mesh, avoiding grid deformation and significantly reducing computational cost. The simulated freight train was configured with a 35 t axle load, a bogie wheelbase of 1.86 m, and a centre-to-centre distance of 1.94 m between adjacent bogies.

3.2 Characteristics of stress distribution on the sub-ballast surface

To investigate the dynamic stress distribution on the sub-ballast and engineered subgrade surfaces under varying train positions, and to assess the impact of the discrete sleeper arrangement along the direction of travel on substructure stress, the longitudinal centre of the model was designated as the coordinate origin (x = 0 m). Along the direction of travel (x-direction), dynamic stress values on both the sub-ballast and engineered subgrade surfaces were simultaneously extracted at four representative wheel load positions: directly above the sleeper, at the mid-point between sleepers, at one-quarter, and at one-eighth of the distance between sleepers. The corresponding stress distribution patterns are shown in Figure 6.

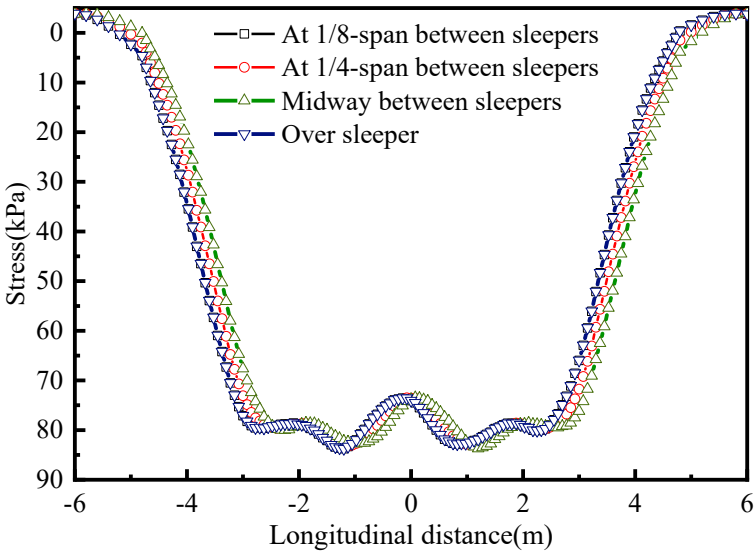

(a)

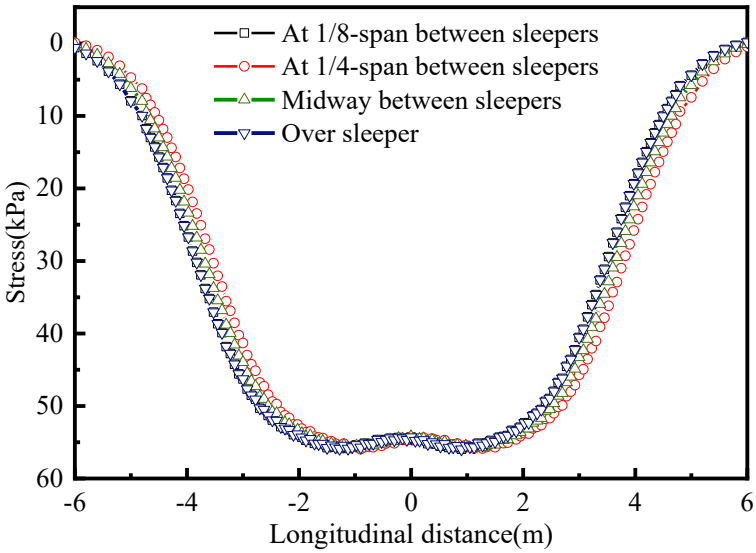

(b)

Figure 6. Dynamic stress distribution corresponding to various wheel load positions: (a) Sub-ballast surface; (b) Engineered subgrade surface.

When the first wheel load was applied directly above the sleeper, at the mid-point between sleepers, at one-quarter, and at one-eighth of the distance between sleepers, the corresponding peak dynamic stresses on the sub-ballast surface were 86.09 kPa, 85.99 kPa, 85.58 kPa, and 86.09 kPa, respectively. The variation in peak stress across these loading positions was minimal, with a maximum of 86.09 kPa and a minimum of 85.58 kPa. Relative to the reference stress beneath the sleeper (86.09 kPa), the peak stress deviations at the mid-point, one-quarter, and

one-eighth positions were 0.11%, 0.58%, and 0%, respectively. For the engineered subgrade surface, the corresponding peak dynamic stresses were 55.97 kPa, 55.96 kPa, 55.92 kPa, and 55.97 kPa. Taking the stress beneath the sleeper (55.97 kPa) as the reference, the relative deviations at the mid-point, one-quarter, and one-eighth positions were 0.05‰, 0.09%, and 0%, respectively. These results confirm that all relative deviations are less than 0.6%, demonstrating that the peak dynamic stress and overall distribution pattern within the subgrade structure are highly consistent across different wheel load positions. The negligible sensitivity of the stress distribution to wheel load position further verifies the accuracy and applicability of the proposed sub-ballast surface loading model.

3.3 Loading pattern on the sub-ballast surface

Finite element simulations indicate that the sub-ballast surface stress exhibits a multi-peak distribution along the longitudinal (x) direction and a twin-peak pattern in the transverse (y) direction. The coordinate origin is defined at the projection point on the sub-ballast surface corresponding to the centre of the two rails and the four-axle loading arrangement. A simplified three-dimensional schematic illustrating the substructure configuration subjected to four-axle loading, along with the corresponding coordinate system, is presented in Figure 7.

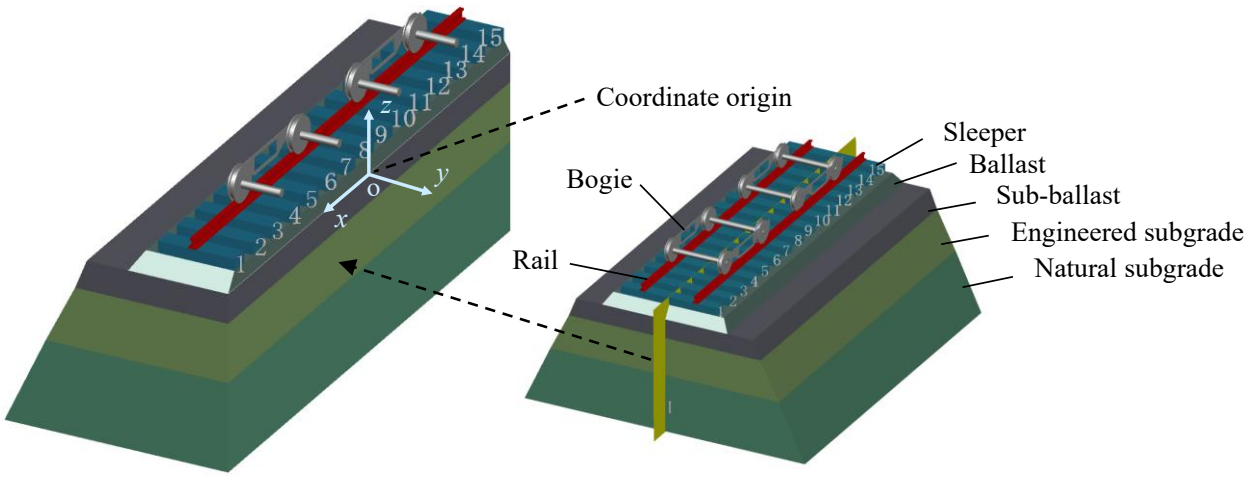

Figure 7. Coordinate system and structural configuration of the heavy-haul railway subgrade model

The transverse stress at the position of the second wheel load, along with the longitudinal stress directly beneath the rail, were analysed using curve fitting techniques. The results demonstrate that the stress distribution on the sub-ballast surface conforms to a pattern governed

by the superposition of Gaussian functions. The fitted curves corresponding to both the transverse and longitudinal stress components are illustrated in Figure 8.

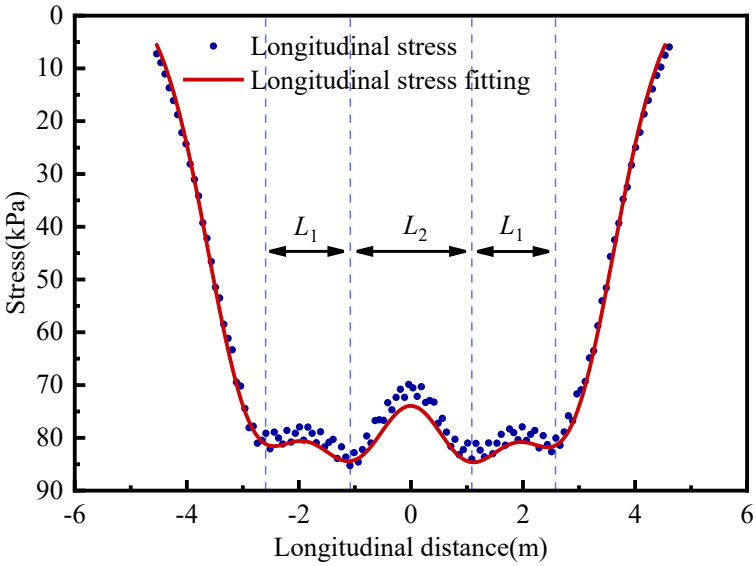

(a)

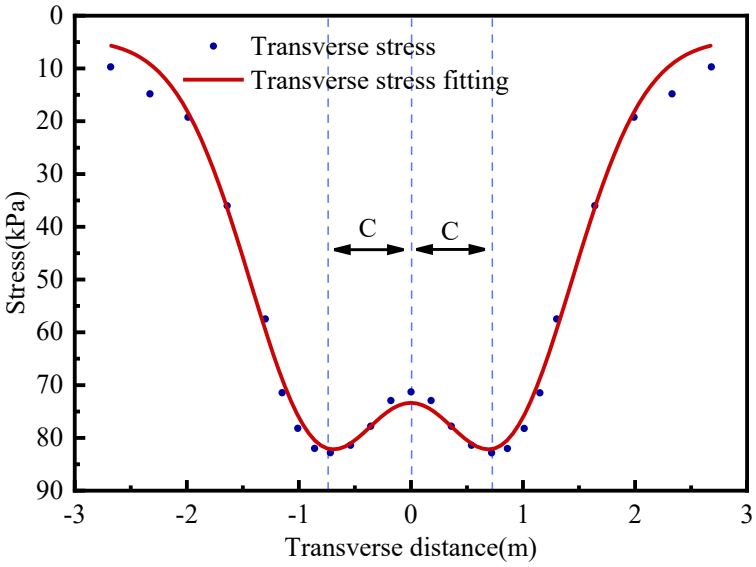

(b)

Figure 8. Fitted curves of transverse and longitudinal sub-ballast surface stress: (a) Longitudinal; (b) Transverse

The stress distribution function along the direction of travel on the sub-ballast surface, directly beneath the rail, is defined by Equation (12).

$$\sigma_x = F(x) = f_1(x) + f_2(x) + f_3(x) + f_4(x) + 0.084(1+\alpha v)T \tag{12}$$

where σ_x denotes the sub-ballast surface stress directly beneath the rail in the direction of

travel; the functions $f_1(x)$、$f_2(x)$、$f_3(x)$、$f_4(x)$ are defined in Equation (13).

$$\begin{cases} f_1(x) = -1.932(1+\alpha v)T\sqrt{\frac{2}{\pi}}e^{-2\left(\frac{x+\mathrm{A}}{1.7}\right)^2} \\ f_2(x) = -1.932(1+\alpha v)T\sqrt{\frac{2}{\pi}}e^{-2\left(\frac{x+\mathrm{B}}{1.7}\right)^2} \\ f_3(x) = -1.932(1+\alpha v)T\sqrt{\frac{2}{\pi}}e^{-2\left(\frac{x-\mathrm{B}}{1.7}\right)^2} \\ f_4(x) = -1.932(1+\alpha v)T\sqrt{\frac{2}{\pi}}e^{-2\left(\frac{x-\mathrm{A}}{1.7}\right)^2} \end{cases} \tag{13}$$

wherein A=L_1+L_2/2 and B=L_2/2, with L_1 and L_2 denoting the bogie wheelbase and bogie spacing, respectively. T denotes the axle load of the train, α represents the speed impact factor, and v denotes the operating speed of the train, expressed in km/h. According to the China Academy of Railway Sciences, for seamless heavy-haul tracks, α=0.004[44].

The transverse stress distribution function beneath the second wheelset is expressed as Equation (14):

$$\sigma_y = G(y) = g_1(y) + g_2(y)\text{-}0.106(1+\alpha v)T \tag{14}$$

with the component functions g_1(y) and g_2(y) defined in Equation (15).

$$\begin{cases} g_1(y) = -1.892(1+\alpha v)T\sqrt{\frac{2}{\pi}}e^{-2\left(\frac{y+C}{1.29}\right)^2} \\ g_2(y) = -1.892(1+\alpha v)T\sqrt{\frac{2}{\pi}}e^{-2\left(\frac{y-C}{1.29}\right)^2} \end{cases} \tag{15}$$

Here, C=0.797 m represents approximately half the distance between the two rails, and σ_y denotes the transverse sub-ballast surface stress at the location of the second wheel load.

Based on the longitudinal and transverse stress distribution functions, the resulting stress distribution on the sub-ballast surface is defined as Equation (16):

$$\sigma_v = s(x,y) = \frac{\sigma_x \cdot \sigma_y}{\left(\sigma_{xy}\right)_{\max}} \tag{16}$$

where σ_v denotes sub-ballast surface stress, while $(\sigma_{xy})_{\max}$ represent the maximum sub-ballast surface stresses.

3.4 Validation

To assess the validity and reliability of the proposed sub-ballast surface loading model, a comparative evaluation was performed based on the sleeper load-sharing ratio proposed by Lv

et al.[35]. This ratio characterises the proportion of wheel load distributed to individual sleepers via the rails, providing insight into the load transfer mechanism and its subsequent impact on the stress state within the subgrade. For example, when a single wheel load *P* is applied directly above a sleeper, it is distributed among five adjacent sleepers with the proportions of 9.24%, 24.14%, 33.24%, 24.14%, and 9.24%, respectively. This distribution is symmetric, with the central sleeper bearing the highest load, which gradually decreases towards the sides. The sleeper load-sharing ratio not only determines the relative loading on each sleeper but also affects the stress distribution within the substructure. Accurate determination of sub-ballast surface stress distribution necessitates consideration of the superposition effects resulting from the superposition of multiple axle loads. The integration of sleeper load-sharing ratios allows for explicit modelling of the stress field induced beneath each sleeper, forming the theoretical basis for deriving the corresponding sub-ballast surface stresses.

Figure 9 presents the sleeper load-sharing ratios for vehicles with axle loads of 30 t and 35 t at various longitudinal positions.

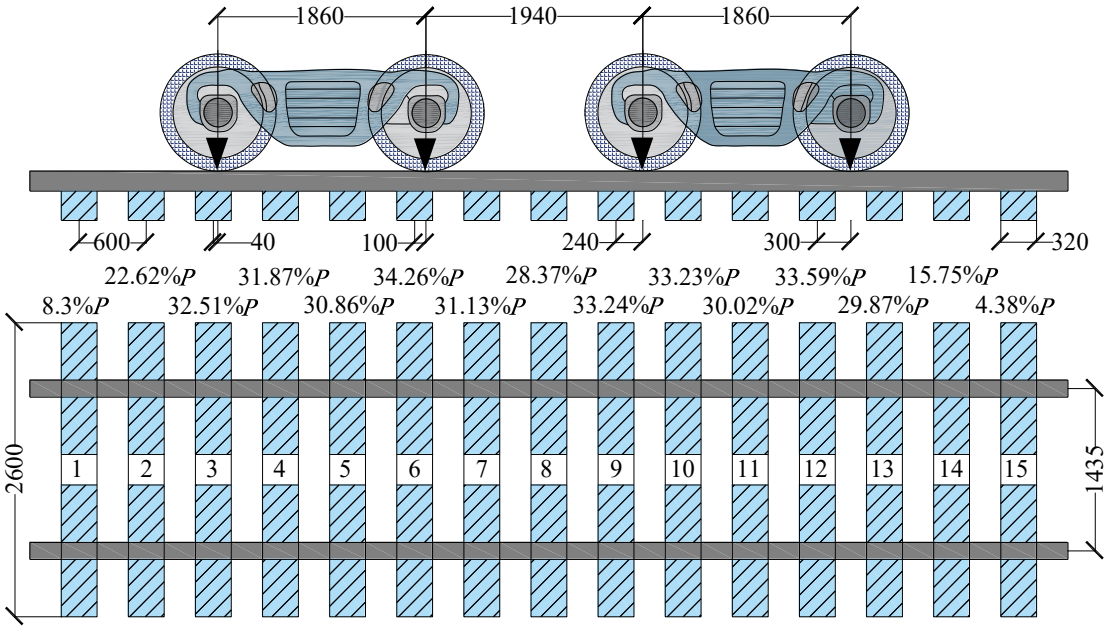

(a)

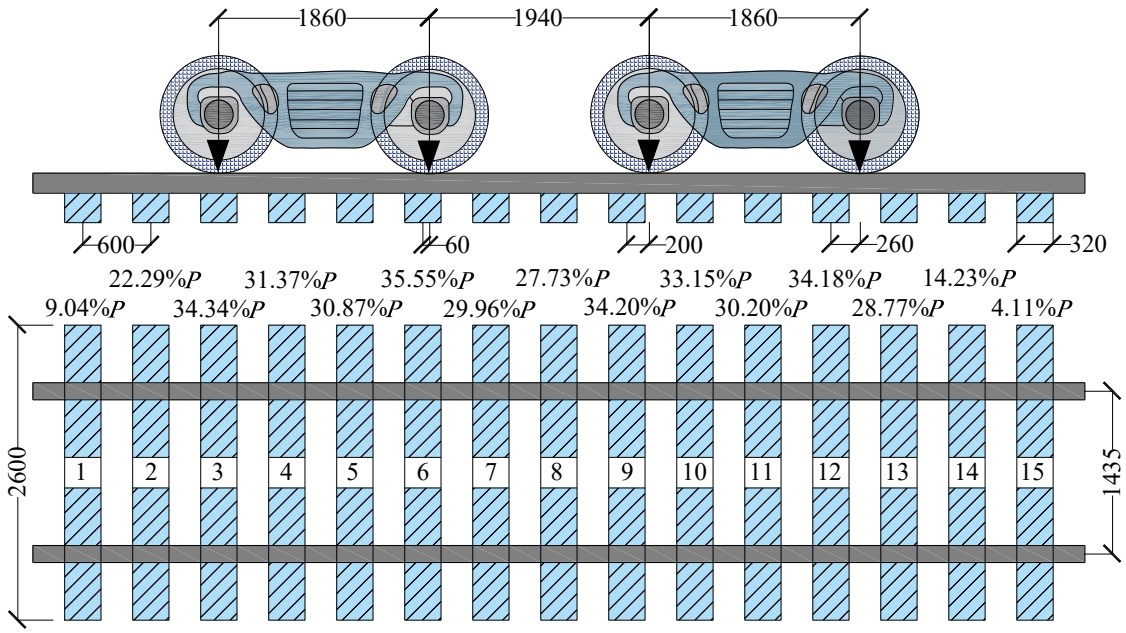

(b)

Figure 9. Sleeper load-sharing ratios subjected to four-axle loading: (a) 30 t axle-load freight vehicle, load applied at the critical rail position; (b) 35 t axle-load freight vehicle, first wheel load positioned directly above a sleeper (Units: mm)

Figure 10 presents the longitudinal stress distribution curves and corresponding fitted curves beneath the rails and at the midpoint between the rails for both vehicle types.

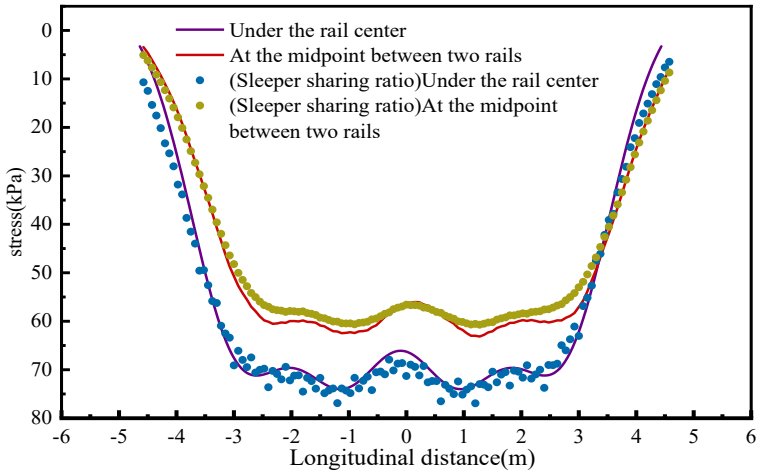

(a)

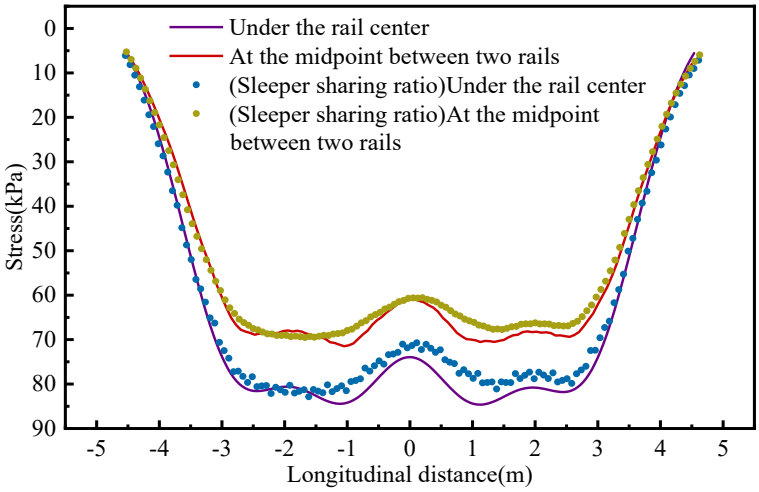

(b)

Figure 10. Comparison of longitudinal stress distribution on the sub-ballast surface: (a) 30 t axle load; (b) 35 t axle load

For the 30 t axle-load freight vehicle, the peak stress beneath the rail obtained from the finite element analysis is 74.0 kPa, while the sleeper load-sharing method yields a corresponding value of 76.9 kPa, resulting in a relative difference of 3.9%. At the midpoint between the rails, the corresponding peak values are 63.4 kPa and 60.7 kPa, with a relative gap of 4.3%. For the 35 t axle-load freight vehicle, the peak stress beneath the rail obtained from the finite element model is 84.6 kPa, while the value calculated using the load-sharing method is 82.8 kPa, resulting in a relative difference of 2.1%. At the midpoint between the rails, the peak values are 71.5 kPa and 69.5 kPa, with a relative gap of 2.8%. All relative errors are within 5%, and the stress distribution curves exhibit excellent agreement in shape, confirming that the proposed four-axle loading model closely approximates the load-sharing method and accurately represents longitudinal stress.

Figure 11 presents the depthwise attenuation of stress beneath the rails and at the midpoint between the rails.

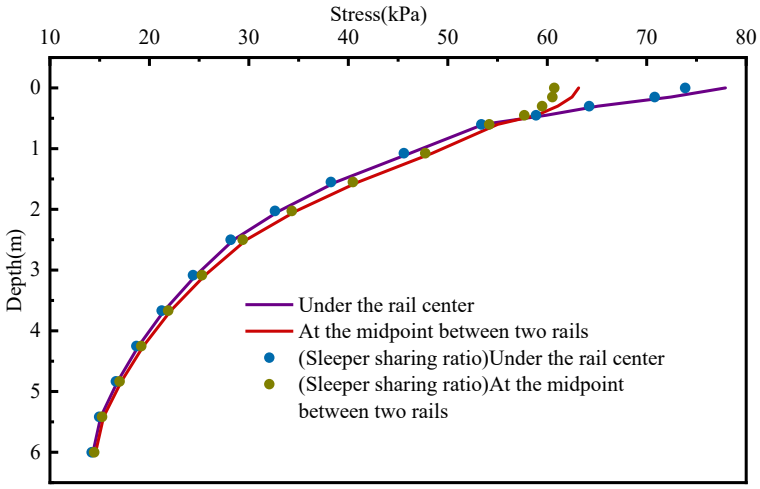

(a)

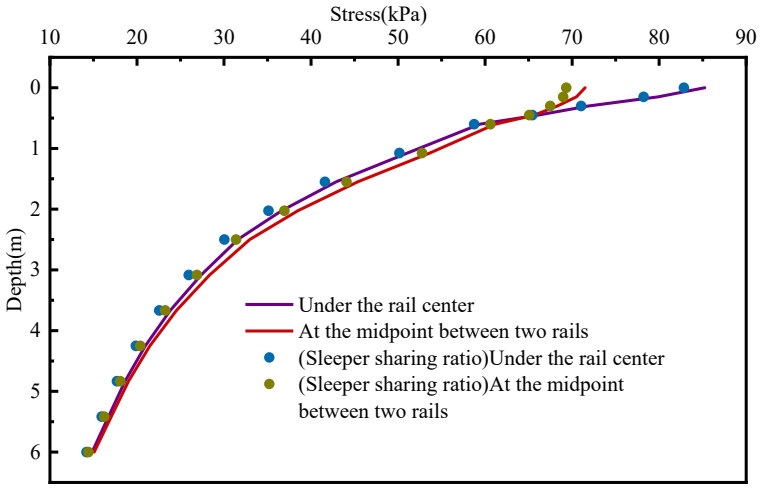

(b)

Figure 11. Depthwise stress attenuation beneath the rail and at the midpoint between the rails: (a) 30 t axle-load; (b) 35 t axle-load

At a depth of 0 m, the stress beneath the rail for the 30 t axle-load vehicle measures 76.9 kPa using the finite element method, compared to 73.9 kPa derived from the sleeper load distribution technique, indicating a relative difference of 4.0%. At the midpoint between the rails, the corresponding values are 63.2 kPa and 60.7 kPa, with a relative gap of 3.9%. For the 35 t axle-load vehicle, the stress values beneath the rail obtained by the two methods are 84.00 kPa and 80.39 kPa, respectively, resulting in a relative gap of 2.1%; at the midpoint between the rails, the values are 71.5 kPa and 69.3 kPa, with a relative gap of 3.1%. With increasing depth (3–6 m), the stress curves show a rapid-to-gradual attenuation pattern that stabilises. Relative errors remain consistently within 5%. These findings demonstrate that the proposed loading

model closely aligns with the load-sharing method on the surface and accurately reflects the depth-dependent attenuation of dynamic stresses reported in existing literature.

4. Shakedown limit analysis of ballasted tracks

Based on the analytical framework for shakedown assessment established in the preceding sections, and in accordance with the *Heavy-Haul Railway Design Code* (TB 10625-2017) [41], a multilayered structural model was developed to compute the shakedown limit of heavy-haul railway substructures. These substructures typically comprise three main layers: the sub-ballast, the engineered subgrade, and the natural subgrade. A semi-structured symmetric model was adopted for the simulation. To improve computational accuracy, mesh refinement was applied to a central region influenced by longitudinal and transverse stress distribution characteristics on the sub-ballast surface. This refined area was identified as the moving load application zone, facilitating an accurate assessment of the elastic stress field within each structural layer. The simplified stress transfer pattern within the substructure is illustrated in Figure 12.

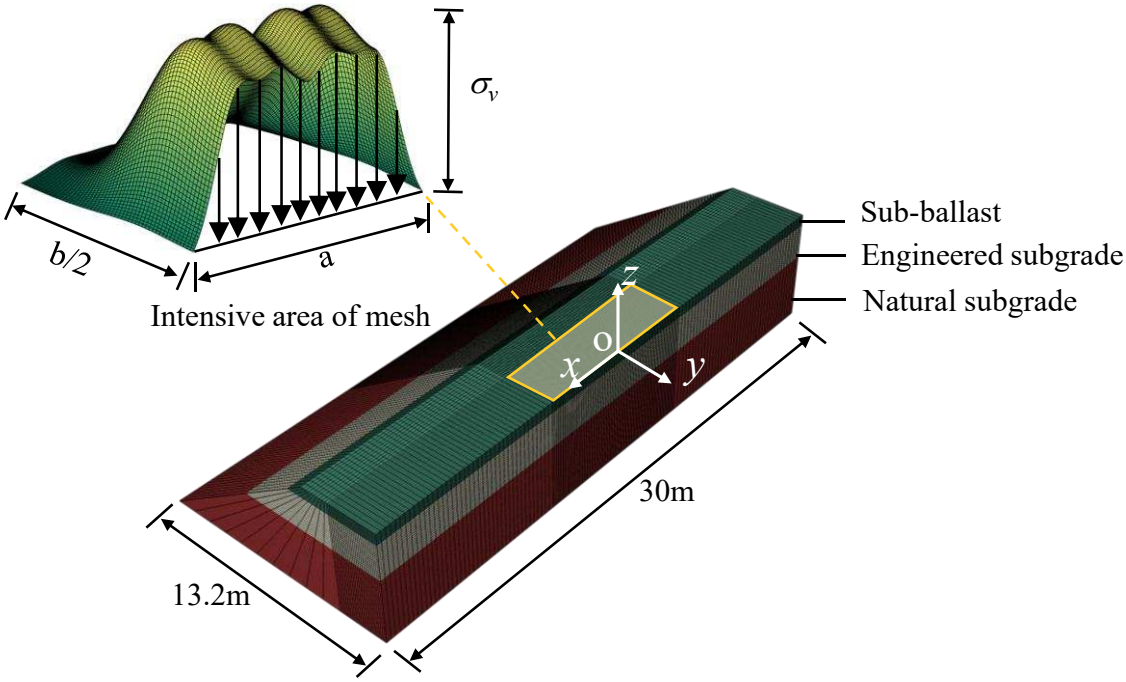

Figure 12. Simplified stress pattern on the sub-ballast surface of a layered structure

The material properties adopted for the reference scenario are summarised in Table 2[38]. To further explore the effects of key design parameters, including the thickness ratio between the sub-ballast and engineered subgrade and the elastic modulus of the engineered subgrade, a series of variable working conditions were defined, as presented in Table 3. Across all scenarios,

the total combined thickness of the sub-ballast and engineered subgrade layers was uniformly maintained at 3.0 m to ensure consistency in structural configuration.

Table 2. Material parameters of the reference case

Components	Density (kg/m^3)	Thickness (m)	Modulus (MPa)	Poisson's Ratio	Cohesion (kPa)	Friction angle (°)
Sub-ballast	2,300	h_1=0.7	E_1=180	0.3	1	φ=35
Engineered subgrade	2,200	h_2=2.3	E_2=150	0.3	1	40
Natural subgrade	1,800	3.5	60	0.35	5	35

Table 3. Material parameters of variable cases

Friction angle φ (°)	25		30		35		40
E_1 (MPa)	180	180	180	180	180	180	180
E_2 (MPa)	120	130	140	150	160	170	180
h_1 (m)	0.7	0.9	1.1	1.3	1.5	1.7	
h_2 (m)	2.3	2.1	1.9	1.7	1.5	1.3	
$h=h_1/h_2$	0.30	0.43	0.58	0.77	1.00	1.31	

4.1 Effect of sub-ballast internal friction angle

Figure 13 presents the variation in shakedown limit and critical depth as a function of the internal friction angle of the sub-ballast, under different sub-ballast to engineered subgrade thickness ratios and varying elastic moduli of the engineered subgrade.

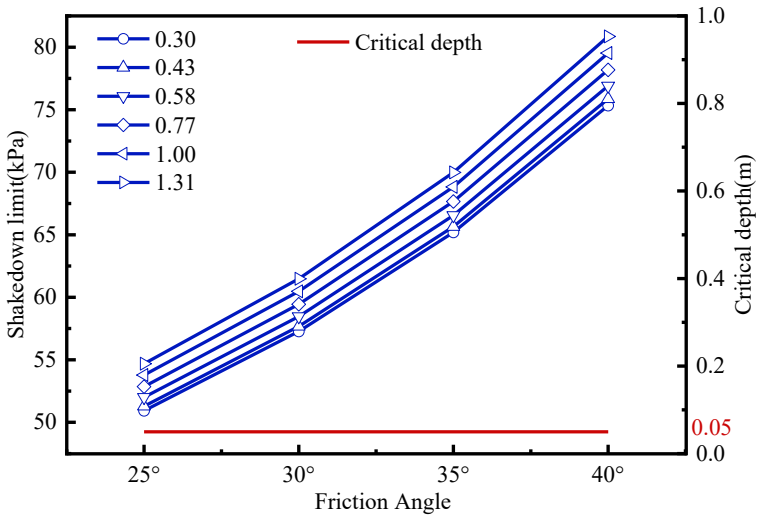

(a)

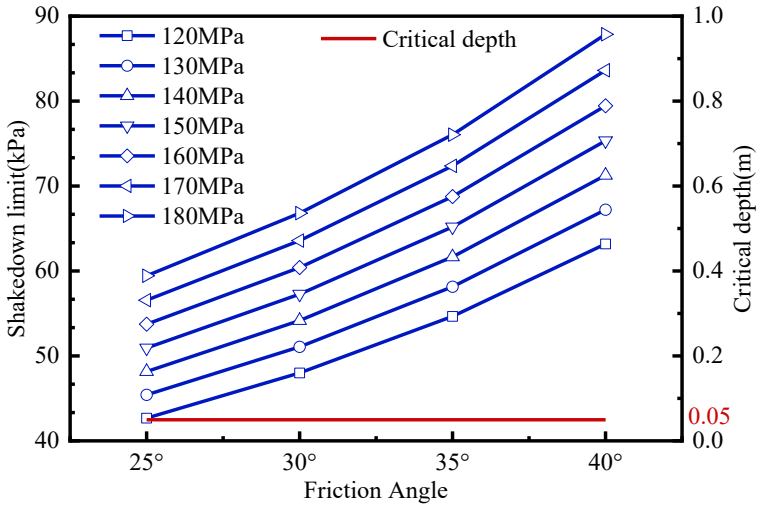

(b)

Figure 13. Effect of sub-ballast friction angle on shakedown limit and critical depth: (a) E_2=150 MPa; (b) h_1/h_2=0.30

Across all examined scenarios, the shakedown limit exhibits a positive correlation with the internal friction angle. For instance, increasing the internal friction angle from 25° to 40° results in the shakedown limit rising from 50.9 kPa to 75.3 kPa at a thickness ratio of 0.30, marking an increase of 47.9%. A similar 47.9% enhancement is observed when the thickness ratio is 1.31. For the engineered subgrade elastic moduli of 120 MPa and 180 MPa, the corresponding increases are 48.0% and 47.9%, respectively. These results underscore that increasing the sub-ballast's internal friction angle significantly augments the structural shear resistance, thereby substantially improving the overall shakedown performance.

In every scenario examined, the critical depth consistently remains at 0.05 m, indicating

that the zone most susceptible to failure lies close to the sub-ballast surface. This observation further underscores the predominant influence of surface strength parameters on shakedown behaviour. Consequently, elevating the internal friction angle of the sub-ballast emerges as an effective means to improve local shear resistance, thereby reinforcing the long-term stability of the substructure.

4.2 Effect of engineered subgrade elastic modulus

Figure 14 depicts the variation in shakedown limit and critical depth as functions of the engineered subgrade's elastic modulus, examined under varying internal friction angles of the sub-ballast.

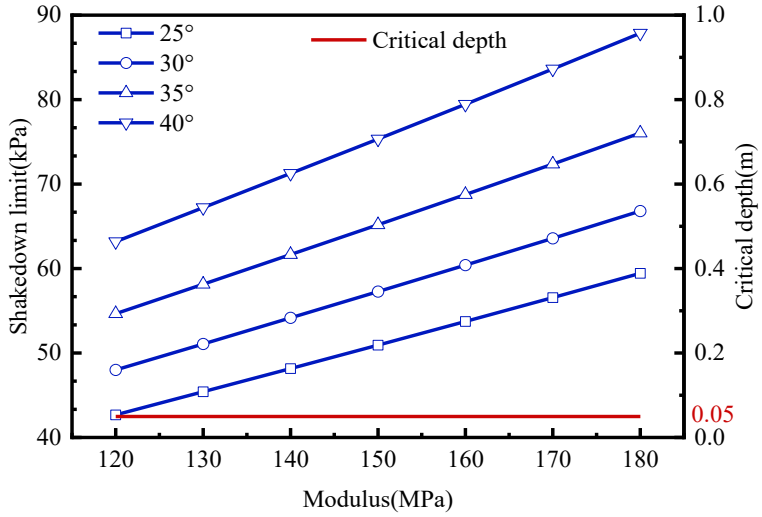

Figure 14. Influence of engineered subgrade elastic modulus on shakedown limit and critical depth.

Across all examined cases, the shakedown limit increases linearly with the elastic modulus of the engineered subgrade. For example, when the sub-ballast internal friction angle is 25°, raising the elastic modulus from 120 MPa to 180 MPa elevates the shakedown limit from 42.68 kPa to 59.44 kPa, corresponding to a 39.3% increase. For an internal friction angle of 40°, a comparable increase of 39.1% is observed. These findings suggest that, regardless of the sub-ballast's internal friction angle, an increased modulus in the engineered subgrade positively influences the shakedown limit, while the rate of this enhancement remains relatively consistent.

The critical depth consistently approaches zero, indicating that the near-surface region

of the sub-ballast is the structurally weakest zone. While increasing the elastic modulus of the engineered subgrade does not directly enhance the shear resistance of the sub-ballast, it reduces the stiffness contrast between layers, thereby improving their mechanical compatibility and indirectly increasing the structural shakedown limit. Furthermore, the influence of the engineered subgrade's elastic modulus on the shakedown limit is comparatively less significant than that of the sub-ballast's internal friction angle, highlighting the greater significance of the latter in improving structural stability. Nevertheless, both parameters remain critical in improving the structure's resistance to plastic failure.

4.3 Effect of sub-ballast to engineered subgrade thickness ratio

Figure 15 illustrates how the shakedown limit and critical depth of heavy-haul railway substructures vary with changes in the thickness ratio between the sub-ballast and engineered subgrade, examined under different internal friction angles of the sub-ballast.

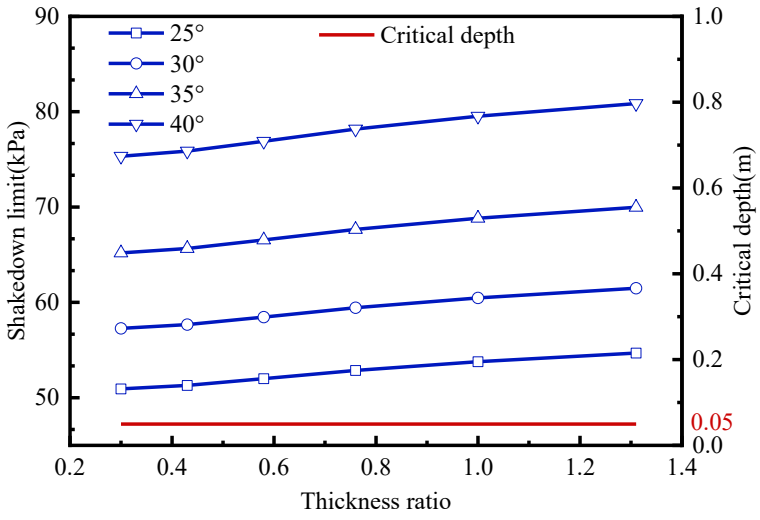

Figure 15. Influence of sub-ballast to engineered subgrade thickness ratio on shakedown limit and critical depth.

Under all examined conditions, the shakedown limit exhibits low sensitivity to changes in the sub-ballast to engineered subgrade thickness ratio, with only modest overall variation. At an internal friction angle of 25° , elevating the thickness ratio from 0.30 to 1.31 causes the shakedown limit to increase from 50.9 kPa to 54.7 kPa, corresponding to a 7.4% rise. For an internal friction angle of 40°, the corresponding increase is 7.3%. This trend indicates that, although increasing the thickness ratio enhances the overall stiffness of the sub-ballast, owing

to its higher modulus relative to the engineered subgrade, its influence on shakedown performance remains limited.

Moreover, the critical depth consistently approaches zero across all scenarios, reaffirming that the structurally weakest region is concentrated near the sub-ballast surface. Although a moderate increase in sub-ballast thickness can slightly enhance structural stiffness, its influence on shakedown performance is minimal compared to the effects of changes in the sub-ballast's internal friction angle and the engineered subgrade's elastic modulus.

4.4 Shakedown axle load

According to the sub-ballast surface stress expression in Equation (16), the shakedown limit can be translated into the equivalent shakedown axle load, denoted as P_0, providing a more intuitive representation of the allowable train loads [7]. The shakedown axle load is determined using Equation (17).

$$(\lambda P_0)_{al} = \frac{\lambda T(1+\alpha v)}{\sigma_v} \tag{17}$$

Where $(\lambda P_0)_{al}$ denotes the shakedown axle load under four-axle loading, expressed in tonnes (t).

The variation in shakedown axle load under standard operating conditions with respect to train speed is illustrated in Figure 16.

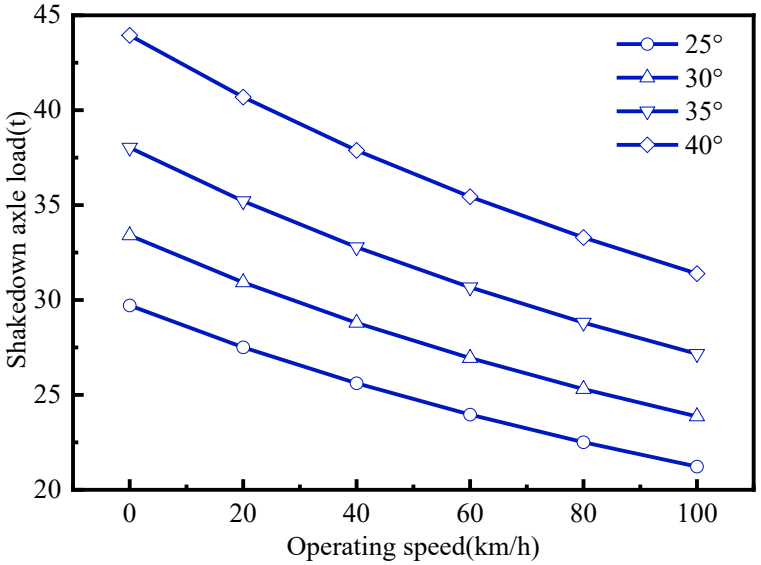

Figure 16. Variation of shakedown axle load with speed

Under varying internal friction angles, the shakedown axle load exhibits an exponential decay with increasing speed. At a train speed of 80 km/h, increasing the internal friction angle

increases from 25° to 40° results in shakedown axle loads of 22.5 t, 25.3 t, 28.8 t, and 33.3 t, with respective increases of 12.4%, 13.8%, and 15.6% for every 5° increment. This trend remains consistent at 100 km/h, confirming that higher internal friction angles significantly enhance structural shakedown performance, with a more pronounced effect than other parameters.

Figure 17 depicts the variation of the shakedown axle load with train speed under varying elastic moduli of the engineered subgrade and different sub-ballast to engineered subgrade thickness ratios, while maintaining the sub-ballast internal friction angle constant at 35° .

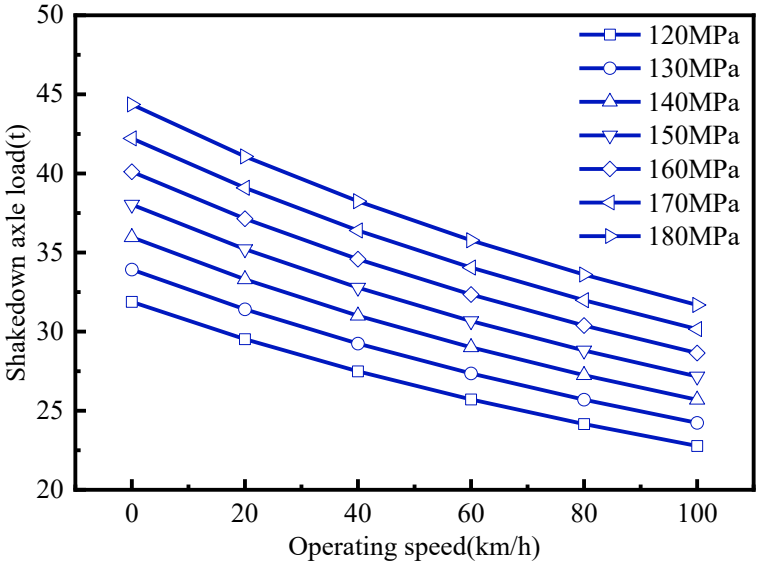

(a)

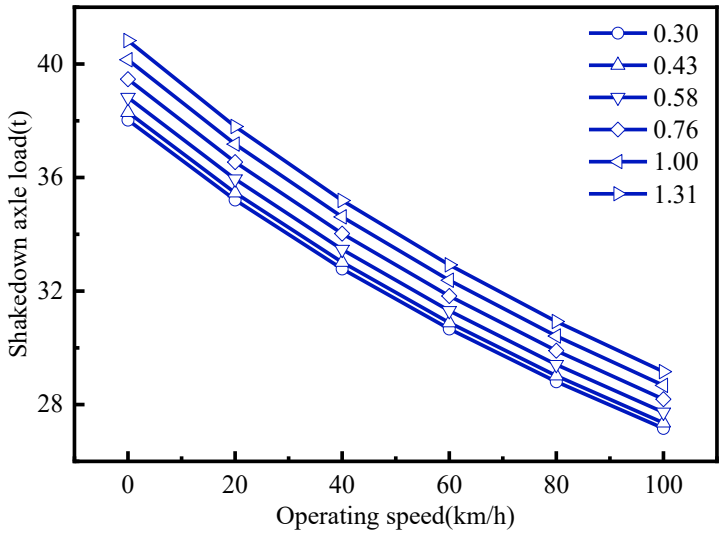

(b)

Figure 17. Influence of speed on shakedown axle load: (a) h_1/h_2=0.30; (E_2); (b) E_2=150

MPa

At 80 km/h, increasing the elastic modulus of the engineered subgrade from 120 MPa to 180 MPa results in shakedown axle loads of 24.2to 33.6 t, with percentage increases of 6.4%, 6.0%, 5.7%, 5.5%, 55.3%, and 5.1% for each 10 MPa increment. This trend is consistent at higher speeds, indicating a gradually diminishing influence of the modulus on shakedown performance. Similarly, increasing the thickness ratio from 0.30 to 1.3, corresponding to an increase in sub-ballast thickness from 0.7 m to 1.7 m at intervals of 0.2 m, produces shakedown axle loads ranging from 17.9 t to 26.5 t, with incremental changes of 0.7%, 1.4%, 1.7%, 1.7%, and 1.7%. This trend remains stable across different speeds, suggesting that the contribution of the thickness ratio is modest and tends to stabilise.

In summary, the shakedown axle load decays in an inverse proportion to increasing train speed across all conditions. Under standard conditions, with an internal friction angle of the sub-ballast of 35°, increasing this angle by 5°, the modulus of the engineered subgrade by 10 MPa, or the thickness of the sub-ballast by 0.2 m results in shakedown axle load increases of approximately 15.6%, 5.5%, and 0.7%, respectively. These results demonstrate that enhancing the internal friction angle of the sub-ballast exerts the greatest influence on shakedown performance, followed by the modulus of the engineered subgrade, with the thickness ratio playing a relatively minor role. Therefore, in optimising the design of heavy-haul railway substructures, priority should be given to improving the shear strength of sub-ballast materials.

4.5 Implications for substructure design

According to the above analysis, the shakedown limit varies under different conditions of sub-ballast internal friction angle, engineered subgrade elastic modulus, and sub-ballast to engineered subgrade thickness ratio. Given the consistent relationship between the shakedown axle load and the shakedown limit, it is necessary to accurately quantify the influence of each parameter on the shakedown axle load. To this end, normalization factors[45] $X_{\lambda(\varphi)}$, $X_{\lambda(E_2)}$ and $X_{\lambda(h_1/h_2)}$ related to the shakedown limit are introduced based on the results presented in Figures 13, 14 and 15.

The influence of the sub-ballast internal friction angle, φ, on the shakedown limit is

captured by Equation (18):

$$X_{\lambda(\varphi)} = \frac{\lambda(\varphi, E_2) - \lambda(25, E_2)}{\lambda(40, E_2) - \lambda(25, E_2)} \tag{18}$$

where $\lambda(25,\ E_2)$ and $\lambda(40,\ E_2)$ represent the normalized shakedown limits corresponding to sub-ballast internal friction angles of 25° and 40°, respectively.

The influence of the engineered subgrade elastic modulus, E_2, on the shakedown limit is defined by Equation (19):

$$X_{\lambda(E_2)} = \frac{\lambda(E_2, \varphi) - \lambda(120, \varphi)}{\lambda(180, \varphi) - \lambda(120, \varphi)} \tag{19}$$

where $\lambda(120,\ \varphi)$ and $\lambda(180,\ \varphi)$ represent the shakedown limits corresponding to E_2=120 MPa and E_2=180 MPa, respectively.

The influence of the thickness ratio between the sub-ballast and engineered subgrade, h_1/h_2, on the shakedown limit is described by Equation (20):

$$X_{\lambda(h_1/h_2)} = \frac{\lambda(h_1 / h_2, \varphi) - \lambda(0.30, \varphi)}{\lambda(1.31, \varphi) - \lambda(0.30, \varphi)} \tag{20}$$

In this expression, $\lambda(0.30,\ \varphi)$ and $\lambda(1.31,\ \varphi)$ represent the shakedown limits corresponding to thickness ratios h_1/h_2 of 0.30 and 1.31, respectively.

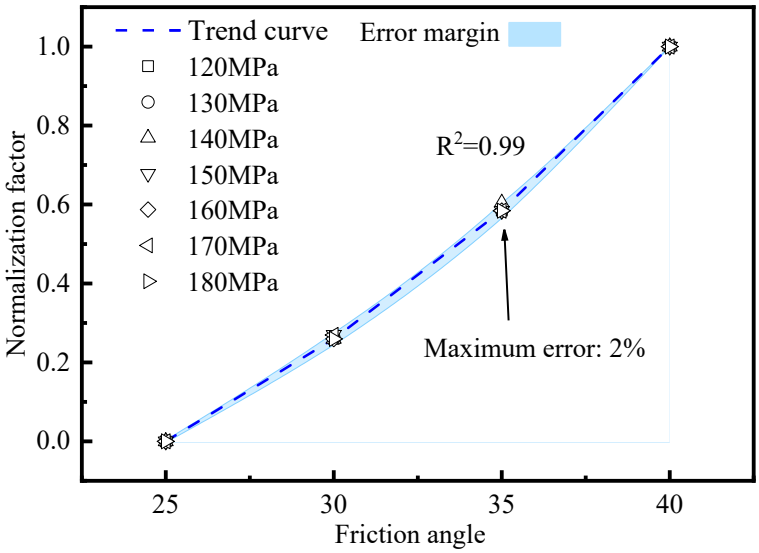

(a)

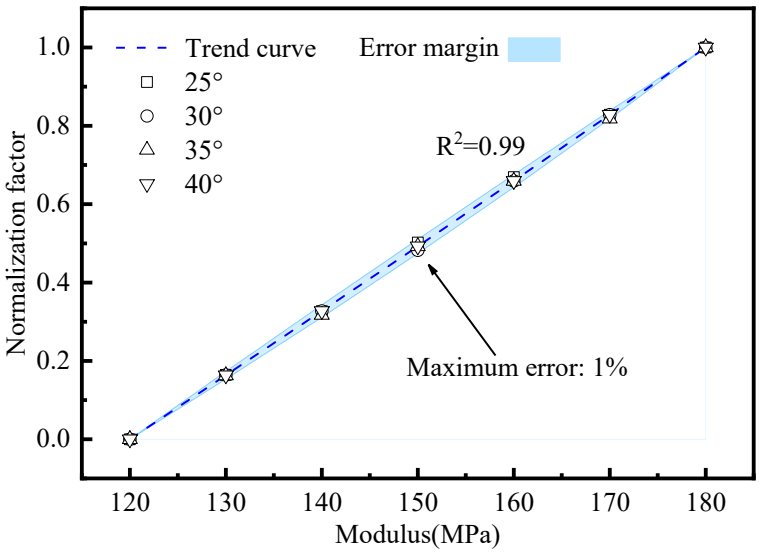

(b)

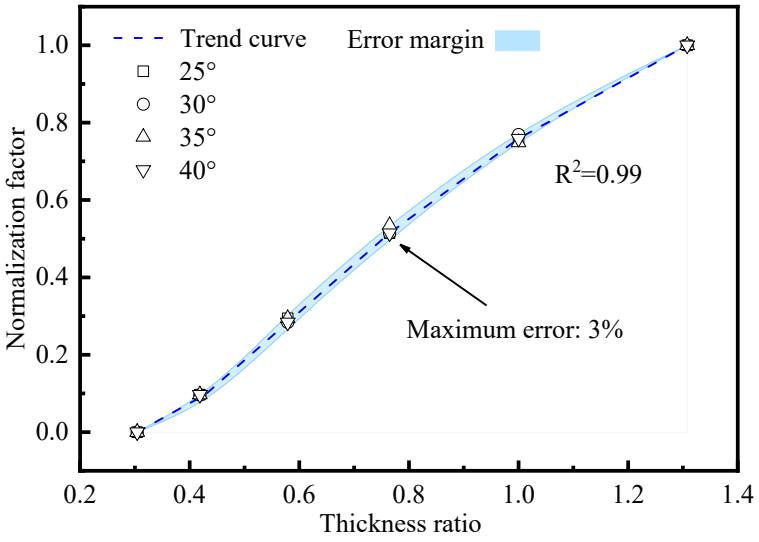

(c)

Figure 18. Relationship between normalization factors and corresponding parameters: (a) Friction angle;(b) Elastic modulus;(c) Thickness ratio

As shown in Equation (18), when φ is constant, the shakedown limits under different values of E_2 are approximately equal, as illustrated in Figure 18(a). Under these conditions, the fitted relationship between the normalization factor $X_{\lambda(\varphi)}$ and φ can be expressed by Equation (21).

$$X_{\lambda(\varphi)} = -(100.19 - 34.96\varphi + 1.56\varphi^2) \cdot 10^{-3} \tag{21}$$

Similarly, as illustrated in Figures 18(b) and 18(c), the fitted relationships between the normalization factors $X_{\lambda(E_2)}$ and $X_{\lambda(h_1/h_2)}$ and their corresponding parameters E_2 and h_1/h_2 are

given by Equations (22) and (23), respectively.

$$X_{\lambda(E_2)} = -(2{,}001.83 + 16.65E_2) \cdot 10^{-3} \tag{22}$$

$$X_{\lambda(h_1/h_2)} = -\left[31.30 + 103.38\left(h_1 / h_2\right)\right] \cdot 10^{-2} \tag{23}$$

Moreover, due to the strong correlation observed between the variation patterns of the shakedown limit and the shakedown axle load, and taking into account the effect of train speed v on the shakedown axle load, all pertinent parameters are consolidated into a unified formulation for the shakedown axle load, as detailed in Equations (24) and (25).

$$\begin{aligned}(\lambda P_0)_{al}\left(\varphi, E_2, v\right) = 1.4T \cdot 10^{-4}(&86{,}650.55 + 2{,}654.41E_2 - 1{,}625.93\varphi - 46.15\varphi E_2 + 72.47\varphi^2 \\ &+2.06\varphi^2 E_2) / [(\sigma_{xy})_{\max}\left(1+\alpha v\right)]\end{aligned} \tag{24}$$

$$\begin{aligned}(\lambda P_0)_{al}\left(\varphi, h_1/h_2, v\right) = 1.4T \cdot 10^{-3}[&47{,}362.99 + 3{,}703.01(h_1/h_2) - 834.75\varphi - 64.03\varphi(h_1/h_2) + 37.21\varphi^2 \\ &+2.85\varphi^2(h_1/h_2)] / [(\sigma_{xy})_{\max}\left(1+\alpha v\right)]\end{aligned} \tag{25}$$

In these expressions, $(\lambda P_0)_{al}\left(\varphi, E_2, v\right)$ represents the shakedown axle load corresponding to a thickness ratio h_1/h_2 =0.30, an internal friction angle φ, an elastic modulus E_2, and a train speed v. Similarly, $(\lambda P_0)_{al}\left(\varphi, h_1/h_2, v\right)$ represents the shakedown axle load for an elastic modulus E_2=150 MPa, an internal friction angle, a thickness ratio h_1/h_2, and a train speed.

Based on Equations (24) and (25), a comparison between the calculated and predicted values of $(\lambda P_0)_{al}\left(\varphi, E_2, v\right)$ and $(\lambda P_0)_{al}\left(\varphi, h_1/h_2, v\right)$ is presented in Figure 19.

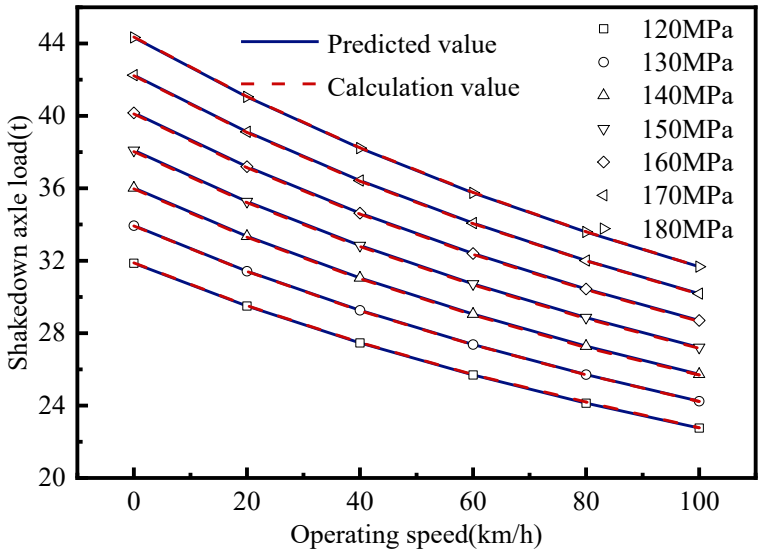

(a)

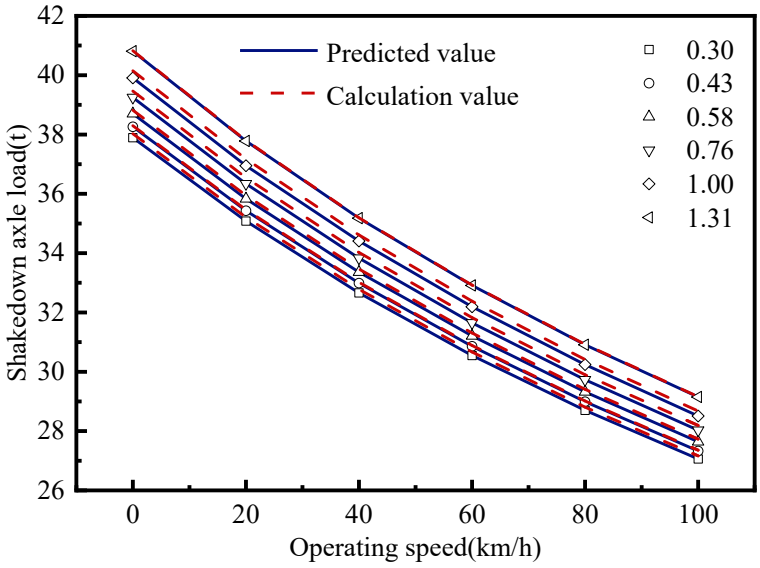

(b)

Figure 19. Comparison of calculated and predicted shakedown limits: (a) h_1/h_2=0.30; (b) E_2=150 MPa

The analysis demonstrates that the predicted values show excellent agreement with the finite element results across a range of parameter combinations, with the maximum deviation remaining below 5%. This confirms the accuracy and broad applicability of the proposed shakedown axle load prediction model. Further results reveal that the shakedown axle load decreases inversely with increasing train speed. This trend remains consistent under varying structural parameters, indicating that train speed is the dominant factor governing the shakedown axle load.

Equation (24) and (25), together with the trends presented in Figure 19, serves to evaluate the impact of substructure dimensional adjustments or material property enhancements on the long-term stability of ballasted heavy-haul railway tracks, as shown in Figure 20. By integrating numerical analysis with parametric sensitivity analysis, this method provides a robust foundation for the optimisation and retrofitting of substructure design. It ensures that the predicted shakedown axle load surpasses the target design axle load, thereby improving the safety and longevity of the railway infrastructure.

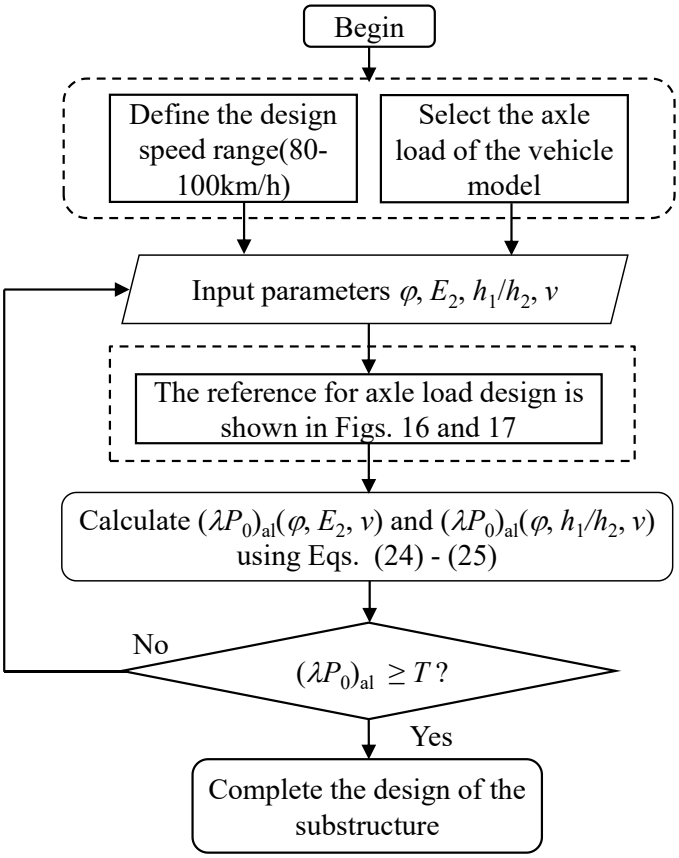

Figure 20. Workflow for estimating shakedown axle load in heavy-haul railway system

5. Conclusions

Building on Melan's lower-bound shakedown theorem, a specialized shakedown analysis model was formulated for multilayer substructures, accompanied by a method to assess the shakedown limit and corresponding shakedown axle load in ballasted track systems. A comprehensive series of parametric studies evaluated the effects of key design parameters, including the internal friction angle of the sub-ballast, the elastic modulus of the engineered subgrade, and the thickness ratio between the sub-ballast and engineered subgrade. The main findings are summarized as follows:

(1) The longitudinal load distribution is characterised by the superposition of four Gaussian functions, while the transverse distribution is formed by the superposition of two Gaussian functions. The longitudinal superposition spacing corresponds to the bogie wheelbase, and the transverse spacing is approximately equal to the track gauge. Moreover, the findings

reveal that, despite the discrete sleeper arrangement along the direction of travel, the stress distribution on the subgrade surface remains continuous and smooth.

(2) Enhancements in the thickness ratio between the sub-ballast and engineered subgrade, the elastic modulus of the engineered subgrade, and the internal friction angle of the sub-ballast all serve to increase the trackbed's shakedown limit. Among these, the internal friction angle of the sub-ballast has the most pronounced effect: increasing it from 25° to 40° results in a maximum rise of 48.0% in the shakedown limit. The elastic modulus of the engineered subgrade has a secondary but linear impact, while the thickness ratio demonstrates minimal influence, rendering it practically negligible in design considerations. These results underscore the internal friction angle of the sub-ballast as the principal parameter governing the substructure's shakedown behaviour.

(3) The shakedown axle load decreases inversely as train speed increases. Enhancements in the sub-ballast's internal friction angle, the engineered subgrade's elastic modulus, and the thickness ratio between the sub-ballast and engineered subgrade collectively contribute to increasing the structure's maximum sustainable axle load. Under typical conditions, with the sub-ballast internal friction angle set at 35°, a 5° increase in this angle, a 10 MPa rise in the engineered subgrade's elastic modulus, and a 0.2 m increment in sub-ballast thickness yield corresponding shakedown axle load increases of 15.6%, 5.5%, and 0.7%, respectively. Moreover, the proposed shakedown axle load expression can reliably predict shakedown axle load values across different parameter configurations, enabling quantitative assessment of the heavy-haul railway subgrade's load-bearing capacity. This provides a solid theoretical foundation and calculation framework for the optimisation and design of subgrade structures.

CRediT authorship contribution statement

Jinglei Liu: Supervision, Methodology, Funding acquisition, Conceptualization. **Shiqi Feng**: Writing – original draft, Writing –review & editing. **Tengfei Wang**: Funding acquisition, Conceptualization. **David P. Connolly**: Review & editing. **Jing Guo**: Supervision. **Erjun Guo**: Validation, Investigation. **Qingzhi Ye**: Methodology, Funding acquisition, Conceptualization, writing–review & editing.

Declaration of competing interest

The authors declare that they have no known competing financial interests or personal relationships that could have appeared to influence the work reported in this paper.

Acknowledgments

This study was supported by the Overseas Expertise Introduction Project for Discipline Innovation ("111 Project", Grant No. B21011), the 2024 Hebei Province Universities and Shijiazhuang City Industry-University-Research Cooperation Project (Grant No. 241790877A), the Research Project of Basic Scientific Research Business Funds of Colleges and Universities in Hebei Province (Grant Nos. 2025ZDTD05, 2025QNJS05) and the Hebei Institute of Architecture and Engineering Doctoral Initiation Fund (Grant No. B-202311).

Data Availability Statement

Data will be made available on request.

References

[1] Lazorenko G, Kasprzhitskii A, Khakiev Z, et al. Dynamic behavior and stability of soil foundation in heavy haul railway tracks: A review. Construct Building Mater. 2019, 205: 111-136. https://doi.org/10.1016/j.conbuildmat.2019.01.184

[2] Liu X, Xiao J, Cai D, et al. Recent advances in subgrade engineering for high-speed railway. Intelligent Transportation Infrastructure, 2023, 2: liad001. https://doi.org/10.1093/iti/liad001

[3] Zhuang Y, Wang K, Li H, et al. Application of three-dimensional shakedown solutions in railway structure under multiple Hertz loads. Soil Dyn Earthq Eng. 2019; 117:328–338. https://doi.org/10.1016/j.soildyn.2018.11.031

[4] Bi Z, Ye Y, Gong Q, et al. An improved thermo-parameters method for dynamic shakedown analysis of railway subgrade. Transp Geotech. 2022; 33:100657. https://doi.org/10.1016/j.trgeo.2021.100657

[5] Lin Y, Zheng J, Fang H, et al. Lower-bound shakedown solutions for transportation infrastructures subjected to moving harmonic loads: A focus on saturated subgrade support. Transp Geotech. 2024; 45:101210. https://doi.org/10.1016/j.trgeo.2024.101210

[6] Sharp R, Booker J. Shakedown of pavements under moving surface loads. J Transp Eng. 1984;110(1):1–14. https://doi.org/10.1016/0148-9062(84)91117-3

[7] Wang T, Connolly D, Luo Q, et al. Shakedown limit analysis of railway slab track foundations under

train loading. Comput Geotech. 2023; 161:105620. https://doi.org/10.1016/j.compgeo.2023.105620

[8] Connolly D, Yu H. A shakedown limit calculation method for geogrid reinforced soils under moving loads. Geotext Geomembr. 2021;49(3):688–696. https://doi.org/10.1016/j.geotexmem.2020.11.009

[9] Tang X, Wang J. A general shakedown approach for geo-structures under cyclic loading using ABAQUS/Python. Acta Geotech. 2022;17(12):5773–5788. https://doi.org/10.1007/s11440-022-01499-4

[10] Wang K, Zhuang Y. Characterizing the permanent deformation response-behavior of subgrade material under cyclic loading based on the shakedown theory. Constr Build Mater. 2021; 311:125325. https:/doi.org/10.1016/j.conbuildmat.2021.125325

[11] Melan E. Der spannungsgudstand eines Henky-Mises schen Kontinuums bei Verlandicher Belastung. Sitzber Akad Wiss Wien. 1938; 147:73.

[12] Radovsky B, Murashina N. Shakedown of subgrade soil under repeated loading. Transp Res Rec. 1996; 1207:181–186. https://doi.org/10.1177/0361198196154700112

[13] Wang J. Shakedown analysis and design of flexible road pavements under moving surface loads [PhD thesis]. University of Nottingham; 2011.

[14] Wang J, Yu H. Residual stresses and shakedown in cohesive-frictional half-space under moving surface loads. Geomech Geoeng. 2013;8(1):1–14. https://doi.org/10.1080/17486025.2012.759281

[15] Brown S, Yu H, Juspi S, et al. Validation experiments for lower-bound shakedown theory applied to layered pavement systems. Géotechnique. 2012;62(10):923–932. https://doi.org/10.1680/geot.11.p.050

[16] Shiau S, Yu H. Load and displacement prediction for shakedown analysis of layered pavements. Transp Res Rec. 2000; 1730:121–129. https://doi.org/10.3141/1730-14

[17] Sun Y, Shen S, Luo C. Shakedown analysis of pavement structures based on lower bound theorem. Rock Soil Mech. 2010;31(11):3667–3670, 3696. (in Chinese) https://doi.org/10.16285/j.rsm.2010.11.016

[18] Yu H. Three-dimensional analytical solutions for shakedown of cohesive-frictional materials under moving surface loads. Proc R Soc A. 2005;461(2059):1951–1964. https://doi.org/10.1098/rspa.2005.1445

[19] Yu H, Wang J. Three-dimensional shakedown solutions for cohesive-frictional materials under moving surface loads. Int J Solids Struct. 2012;49(26):3797–3807. https://doi.org/10.1016/j.ijsolstr.2012.08.011

[20] Wang J, Yu H. Three-dimensional shakedown solutions for anisotropic cohesive-frictional materials under moving surface loads. Int J Numer Anal Methods Geomech. 2014;38(4):331–348. https://doi.org/10.1002/nag.2207

[21] Wang J, Yu H. Shakedown analysis and its application in pavement and railway engineering. Comput Geotech. 2021; 138:104281. https://doi.org/10.1016/j.compgeo.2021.104281

[22] Wang J, Yu H. Shakedown analysis for design of flexible pavements under moving loads. Road Mater Pavement Des. 2013;14(3):703–722. https://doi.org/10.1080/14680629.2013.814318

[23] Qian J, Dai Y, Huang M. Dynamic shakedown analysis of two-layered pavement under rolling-sliding contact. Soil Dyn Earthq Eng. 2020; 129:105958. https://doi.org/10.1016/j.soildyn.2019.105958

[24] Zhuang Y, Wang K. Three-dimensional shakedown analysis of ballasted railway structures under moving surface loads with different load distributions. Soil Dyn Earthq Eng. 2017; 100:296–300. https://doi.org/10.1016/j.soildyn.2017.06.012

[25] Zhuang Y, Wang K, Li H. Shakedown solutions for ballasted track structure under multiple uniform loads. Transp Geotech. 2020; 22:100298. https://doi.org/10.1016/j.trgeo.2019.100298

[26] Wang K, Zhuang Y, Liu H. Shakedown analysis for the evaluation of strength and bearing capacity of multilayered railway structures. Proc Inst Mech Eng F J Rail Rapid Transit. 2018;232(9):2324–2335. https://doi.org/10.1177/0954409718766952

[27] Wang J, Liu S, Yang W. Dynamics shakedown analysis of slab track substructures with reference to critical speed. Soil Dyn Earthq Eng. 2018; 106:1–13. https://doi.org/10.1016/j.soildyn.2017.12.004

[28] Xiao J H, Zhang D, Wang Y H, et al. Cumulative deformation characteristic and shakedown limit of railway ballast under cyclic loading. Bearing Capacity of Roads, Railways and Airfields. CRC Press, 2017: 1899-1904.https://doi.org/10.1201/9781315100333-250

[29] Xiao J, Zhang D, Wei K, et al. Shakedown behaviors of railway ballast under cyclic loading. Construction and building materials, 2017, 155: 1206-1214. https://doi.org/10.1016/j.conbuildmat.2017.07.225

[30] Gomes M B B, Guimarães A C R, dos Santos J T A, et al. Analysis of the Deformability of Railroad Ballast Based on the Concept of the Shakedown Limit. International Conference on Transportation Geotechnics. Singapore: Springer Nature Singapore, 2024: 65-75. https://doi.org/10.1007/978-981-97-8217-8_8

[31] Wang K, Zhuang Y, Kouretzis G, et al. Shakedown analysis of ballasted track structure using three-dimensional finite element techniques. Acta Geotech. 2020; 15:1231–1241. https:/doi.org/10.1007/s11440-019-00818-6

[32] Liu P, Zhai W, Wang K. Establishment and verification of three-dimensional dynamic model for heavy-

haul train–track coupled system. Vehicle System Dynamics, 2016, 54(11): 1511-1537. https://doi.org/10.1080/00423114.2016.1213862

[33] Wang T, Yan Z, Li T, et al. Design methodology for heavy-haul railway track foundations under 40-tonne axle loads. International Journal of Rail Transportation, 2025: 1-16. https://doi.org/10.1080/23248378.2025.2453928

[34] Feng G, Zhang L, Luo Q, et al. Monitoring the dynamic response of track formation with retaining wall to heavy-haul train passage. International Journal of Rail Transportation, 2023, 11(5): 748-766. https://doi.org/10.1080/23248378.2022.2103849

[35] Lv W, Li Q, Liu G, et al. Structural analysis and design method for subgrade bed of heavy haul railway. J China Railw Soc. 2016;38(4):74–81. (in Chinese) https://doi.org/10.3969/j.issn.1001-8360.2016.04.011

[36] Mei H, Leng W, Nie R, et al. Random distribution characteristics of peak dynamic stress on the subgrade surface of heavy-haul railways considering track irregularities. Soil Dyn Earthq Eng. 2019; 116:205–214. https://doi.org/10.1016/j.soildyn.2018.10.013

[37] Liu W, Mei H, Leng W, et al. Numerical analysis of dynamic stress response characteristics of subgrade bed. J China Railw Soc. 2017;39(12):108–117. (in Chinese) https://doi.org/10.3969/j.issn.1001-8360.2017.12.015

[38] Xu F, Yang Q, Liu W, et al. Dynamic stress of subgrade bed layers subjected to train vehicles with large axle loads. Shock Vib. 2018; 2018:2916096. https://doi.org/10.1155/2018/2916096

[39] Tran V, Meguid M, Chouinard L. Three-dimensional analysis of geogrid-reinforced soil using a finite-discrete element framework. Int J Geomech. 2015;15(4):04014066. https://doi.org/10.1061/(ASCE)GM.1943-5622.0000410

[40] Boussinesq J. Applications des Potentials à l'étude de l'équilibre et du mouvement des solides élastiques. Paris: Gauthier-Villars; 1885.

[41] TB 10625-2017. Code for Design of Heavy-Haul Railway. China Railway Publishing House: Beijing; 2017.

[42] Lysmer J, Kuhlemeyer R L. Finite dynamic model for infinite media. Journal of the engineering mechanics division, 1969, 95(4): 859-877.

[43] Lane H, Kettil P, Wiberg NE. Moving finite elements and dynamic vehicle interaction. European Journal of Mechanics-A/Solids, 2008, 27(4): 515-531.https://doi.org/10.1016/j.euromechsol.2007.09.007

[44] Zhang Q, Han Z, Lv B. Structural analysis and design method for subgrade bed of high-speed railway. China Railway Science.2005, (06):55-59. (in Chinese) https://doi.org/10.3321/j.issn:1001-4632.2005.06.011

[45] Du J, Luo Q, Jiang L. Fluidized solidification modification tests on expansive soil and its mixing proportions study. Journal of Zhejiang University (Engineering Science), 2024, 58(10): 2137-2148. (in Chinese) https://doi.org/10.3785/j.issn.1008-973X.2024.10.018